Materials Science & Engineering A 937 (2025) 148452

Contents lists available at ScienceDirect

Materials Science & Engineering A

journal homepage: www.elsevier.com/locate/msea

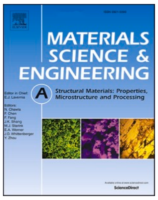

Microstructure evolution and local strengthening mechanisms in CoCrFeMnNi high entropy alloy joints reinforced with Inconel 625

Jiajia Shen [a,b,**], Jin Yang [c], Yeon Taek Choi [d], Rita Gonçalves [a], Rodrigo Pedro [b], D.A. Santana [e], F.G. Coury [e], N. Schell [f], Zhi Zeng [g], Hyoung Seop Kim [d], J.P. Oliveira [a,b,*]

[a] UNIDEMI, Department of Mechanical and Industrial Engineering, NOVA School of Science and Technology, Universidade NOVA de Lisboa, 2829-516, Caparica, Portugal
[b] CENIMAT/I3N, Department of Materials Science, NOVA School of Science and Technology, Universidade NOVA de Lisboa, 2829-516, Caparica, Portugal
[c] School of Materials Engineering, Shanghai University of Engineering Science, Shanghai, 201620, China
[d] Graduate Institute of Ferrous Technology, POSTECH (Pohang University of Science and Technology), Pohang, 790-794, South Korea
[e] Graduate Program in Materials Science and Engineering, Federal University of São Carlos, Rodovia Washington Luís, km 235 SP-310, São Carlos, 13565-905, São Paulo, Brazil
[f] Helmholtz-Zentrum Hereon, Institute of Materials Physics, Max-Planck-Str. 1, Geesthacht, 21502, Germany
[g] School of Mechanical and Electrical Engineering, University of Electronic Science and Technology of China, Chengdu, 611731, China

ARTICLE INFO

Keywords:
CoCrFeMnNi high entropy alloy
Inconel 625
Gas metal arc welding
Synchrotron X-ray diffraction
Thermodynamic calculations
Mechanical testing
Digital image correlation
Strengthening mechanisms

ABSTRACT

In the fusion-based welding processes, filler materials are commonly used to adjust and improve the composition of the fusion zone with the aim of optimizing both microstructure and mechanical properties. However, in the field of welding high entropy alloys, the influence of different filler materials on the microstructure and mechanical response is still scarce, owing to the yet incipient usage of welding technologies for these novel, advanced engineering alloys. To bridge this knowledge gap, Inconel 625 filler wire was used during gas metal arc welding of the well-known CoCrFeMnNi high entropy alloy. To systematically analyze the microstructure evolution and mechanical properties of the welded joints, multiscale characterization techniques were employed. It is shown that the different regions of the welded joint possess distinct microstructural features due to the weld thermal cycle, which is further compounded in the fusion zone by the introduction of the filler material. The use of Inconel 625 filler promotes a solid solution strengthening effect in the fusion zone and became the main contributor to the yield strength of this region (302 MPa (via solid solution strengthening) vs 478 MPa (yield stress from tensile experiments). Since Hall-Petch strengthening is predominant in both base material and heat affected zone, but not on the fusion zone due to the large grain structure that developed, the addition of Inconel 625 filler demonstrates to be a feasible approach to increase the typically low fusion zone strength. By coupling microstructural characterization with mechanical property analysis, aided by the calculation of the strengthening mechanisms, we unveil processing, microstructure, property relationships, providing a broader basis for the widespread application of gas metal arc welding for high entropy alloys.

1. Introduction

Traditional alloys are often composed by one or two principal elements with relatively minor alloying additions of others, so that these can improve the material microstructure and properties. However, with the advancement of science and technology, especially in more complex and extreme environments such as high temperature-, radiation-, and high-speed loading-conditions, structural materials, particularly metallic materials, have been increasingly applied. In order to overcome the limitations of traditional alloys facing these extreme conditions, the concept of high entropy alloys (HEAs) was first proposed by Yeh et al. [1] and Cantor et al. [2] in 2004. These were composed of at least five

---

* Corresponding author. CENIMAT/I3N, Department of Materials Science, NOVA School of Science and Technology, Universidade NOVA de Lisboa, 2829-516, Caparica, Portugal.

** Corresponding author. CENIMAT/I3N, Department of Materials Science, NOVA School of Science and Technology, Universidade NOVA de Lisboa, 2829-516, Caparica, Portugal.

E-mail addresses: j.shen@fct.unl.pt (J. Shen), jp.oliveira@fct.unl.pt (J.P. Oliveira).

https://doi.org/10.1016/j.msea.2025.148452
Received 26 October 2024; Received in revised form 13 April 2025; Accepted 4 May 2025

elements with a composition range between 5 and 35 at. % of each element. The interesting properties displayed by some HEAs make them potentially impactful in fields such as aerospace, molds, tools, corrosion-resistant coatings, and high temperature environments [1,3]. Among the diverse families of high entropy alloys (HEAs), the equiatomic CoCrFeMnNi system stands out for its exceptional fracture toughness and ductility, particularly at cryogenic temperatures, making it a promising candidate for structural applications subjected to thermal cycling or low-temperature environments. On the other hand, complex concentrated alloys (CCAs) or HEAs incorporating refractory elements such as Nb, Mo, Ta, and Hf have been specifically developed for use in extreme high-temperature environments, including aerospace propulsion systems and combustion chambers, where superior oxidation resistance and phase stability are essential. In this regard, NiCrCo-based HEAs have garnered attention as potential substitutes for conventional Ni-based superalloys, such as Inconel series, especially in components demanding high-temperature strength and creep resistance.

Welding, as a widely used joining method, plays a crucial role in the fabrication and assembly of complex-shaped structures. However, when it comes to HEAs, the welding process poses unique challenges due to their complex composition and unknown evolution during the non-equilibrium conditions found in fusion-based welding processes. Understanding the welding behavior and addressing the difficulties associated to welding HEAs is of paramount importance to ensure their successful application in structural engineering.

CoCrFeMnNi HEA have been widely regarded for their outstanding mechanical strength, ductility, fracture toughness, corrosion resistance, and thermal stability, especially under extreme conditions such as cryogenic temperatures and high-temperature environments. These attributes make them promising candidates for a variety of industrial applications, including aerospace structures (e.g., cryogenic fuel tanks, structural frames), cryogenic storage and transportation systems (e.g., LNG tanks, pipelines), energy generation components (e.g., turbines, heat exchangers), chemical and petrochemical processing equipment (e.g., reactors, piping exposed to corrosive environments), nuclear industry components (e.g., cladding materials, internals requiring radiation resistance), and marine engineering structures (e.g., offshore structures requiring corrosion and wear resistance). Successful development of welding techniques for CoCrFeMnNi alloys is thus expected to significantly advance the practical application and structural deployment of HEAs in these critical fields. Currently, research on welding of HEAs has primarily focused on assessing the weldability of the well-known equiatomic CoCrFeMnNi. It has been confirmed that numerous welding methods are applicable to successful weld the CoCrFeMnNi alloy, including gas tungsten arc welding [4], laser beam welding [5–7], electron beam welding [7], and friction stir welding [8,9]. However, in recent years, the addition of filler wires has been increasingly adopted during welding of HEAs to regulate/control the microstructure and enhance the mechanical properties of the joints. The selection of an appropriate filler wire can provide the necessary alloying elements and regulate the alloy composition in the fusion zone through the diffusion and solid solution interactions between the base material and filler wire. This, in turn, affects the microstructure, mechanical and corrosion properties of the welded joint. Considering the current research status regarding the weldability of CoCrFeMnNi HEAs, it has become crucial to investigate the impact of different filler wires on the mechanical properties of these joints.

Regarding this topic, there has been literature reports investigating the influence of using different filler wires on the mechanical response of CoCrFeMnNi joints [10–20], and these studies have been reported to obtain successful heterogeneous welded joints. Specifically, the existing literature demonstrates that while austenitic stainless steel fillers (e.g., STS 308L, STS 304) [10,13,15,17–19] exhibit good structural compatibility with the FCC matrix of CoCrFeMnNi. However, they typically promote the formation of coarse columnar grain structures with limited hardness enhancement (≈150 HV) in the FZ. Autogenous welding with CoCrFeMnNi filler [10,18,20] preserves compositional homogeneity but lacks extrinsic strengthening mechanisms, often necessitating post-weld heat treatment for property enhancement. Dissimilar filler systems, such as duplex stainless steel [10], 304 stainless steels [17], and 316L [13,14], enable joint formation with conventional alloys but introduce interfacial challenges, such as the potential formation of brittle intermetallic phases, which require stringent process control. These studies collectively highlight a key issue: the FZ in dissimilar CoCrFeMnNi welded joints is often the weakest region, exhibiting the lowest hardness and serving as the primary fracture site. Therefore, to addressing this limitation, the present study investigates the use of Inconel 625 as a filler wire, leveraging its high Nb and Mo content – elements with large atomic radii known for their solid solution strengthening effects. This approach is expected to enhance hardness and potentially improve the overall mechanical properties of the welded joint, despite the existence of these studies, there are still relatively limited metallurgical knowledge, especially considering the availability of filler wires with different compositions. Therefore, gaining a deeper understanding of the impact of various filler wires on the performance of CoCrFeMnNi welded joint remains highly significant.

Computational Materials Engineering (CME) has become an indispensable approach in understanding and predicting the microstructural evolution during advanced manufacturing processes, particularly fusion-based welding. Thermodynamic simulations, based on the CALPHAD (CALculation of PHAse Diagrams) methodology and implemented using Thermo-Calc software, enable the prediction of phase stability, solidification paths, and transformation sequences under non-equilibrium conditions. In this study, the Scheil - Gulliver solidification model was employed to simulate the rapid cooling environment inherent to gas metal arc welding (GMAW). This approach assumes complete mixing in the liquid phase and negligible diffusion in the solid phase, thereby effectively approximating the steep thermal gradients and fast solidification rates ($\approx 10^3$–10^4 °C/s) typically encountered during welding. Temperature-dependent phase evolution and critical phase transformation events were predicted to support the interpretation of experimentally observed microstructures, which providing a more comprehensive understanding of solidification and segregation behavior. In addition, the limitations of conventional characterization methods such as SEM/EDS in detecting fine secondary phases were addressed by employing synchrotron radiation-based diffraction techniques for high-resolution phase identification. The integration of computational modeling with experimental validation thus not only supported the interpretation of the microstructural features but also enhanced the overall metallurgical understanding of the solidification pathways, phase stability, and strengthening mechanisms in CoCrFeMnNi - Inconel 625 dissimilar welded joints.

In addition, in the current work, we address this shortcoming to aid in expanding the application potential of CoCrFeMnNi HEA. Thus, Inconel 625 was chosen as the filler wire to investigate its impact on the microstructure and mechanical properties of CoCrFeMnNi welded joints using gas metal arc welding. To comprehensively analyze the microstructure and mechanical properties of the welded joint, a series of multiscale characterization techniques were employed in this study. Characterization methods included optical and electron microscopy, electron backscatter diffraction, high energy synchrotron radiation, and thermodynamic calculations to evaluate and support the microstructural evolution. Additionally, microhardness analysis and digital image correlation (DIC) during tensile testing were conducted to reveal the influence of microstructure (both at micro and macro level) on the observed mechanical performance. The findings obtained from this research contribute to the improve the existing knowledge on the weldability of HEAs and provide valuable insights for the development and optimization of filler-based welding processes for the CoCrFeMnNi system in various engineering applications.

2. Experimental procedures

2.1. Materials

In this study, equiatomic CoCrFeMnNi HEAs were fabricated using vacuum induction melting using elemental raw materials with a minimum purity of 99.9 wt%, with the processing conditions detailed in Ref. [14]. The vacuum level during vacuum induction melting was approximately 5×10^{-3} Pa to minimize contamination. The ingots underwent multiple remelting cycles to ensure good chemical homogeneity. Then, room-temperature cold rolling was employed, which resulted in an approximately 50 % reduction in material thickness, from 3 to 1.5 mm. This condition ultimately was used as the base material. Prior to welding, a rectangular-shaped specimens measuring 60 × 40 × 1.5 mm were cut from the rolled plate using a precision cutting machine. To ensure the cleanliness of the base material prior to welding, 1200-grit SiC papers were utilized to eliminate oxide deposits on the sheet surface and faying surfaces. After that, the samples were cleaned with ethanol and acetone to remove any residual oil or impurities from the cutting and polishing process.

2.2. Gas metal arc welding

In this study, gas metal arc welding (GMAW) was employed to investigate the effects of using Inconel 625 filler wire on the solidification microstructure and mechanical response of CoCrFeMnNi welded joints. The Inconel 625 filler wire used for welding was a commercial product with a certified purity above 99.9 wt%. The composition of both BM and filler material were shown in Table 1.

To ensure fully penetrated and defect-free welded joints, direct current with straight polarity welding was utilized. During the welding process, pure argon (99.99 %) shielding gas was applied to both the face and root of the sheets to prevent oxidation of the heat affected zone (HAZ) and fusion zone (FZ). The final optimal welding process parameters were determined as follows: voltage of 17 V, torch travel speed of 160 mm/min, wire feeding speed of 2000 mm/min and gas flow rate of 16 L/min. The welding direction was set normal to the rolling direction. A schematic depiction of the process is shown in Fig. 1. Following welding, dog-bone shaped specimens were obtained using electrical discharge machining (as illustrated in Fig. 1). These specimens were used to characterize the microstructure and mechanical properties of the welded joint.

2.3. Microstructure characterization

For microstructure characterization, metallographic specimens were prepared following the conventional metallographic sample preparation procedures. Initially, the specimens were mounted in epoxy resin. Then, a sequence of grinding steps was performed using SiC papers with a range of grit sizes from 240 to 4000, followed by polishing with a 0.3 μm diamond paste. Finally, the obtained mirror-like surface was immersed in an etching solution consisting of sulfuric acid and nitric acid (3:1 in volume) for appropriately 20 s and then washed immediately with ethanol to expose the microstructure of the specimen. To observe the microstructure of the welded joints, a combination of different instruments was utilized. These included a Leica DMI 5000 M inverted optical microscope, a JSM-7100F scanning electron microscope (SEM) coupled with electron backscattered diffraction (EBSD). The raw EBSD data were processed using the TSL OIM Analysis 7.0 software to analyze and interpret the microstructure information of the welded joint.

To further investigate the influence of the welding thermal cycle on the microstructural evolution of the whole welded joint, synchrotron X-ray diffraction was employed. This study was conducted at the P07B beamline of PETRAIII/DESY in Germany. The energy used for the synchrotron X-ray diffraction experiments was 87.1 keV, corresponding to a wavelength of 0.14235 Å. The beam size was set at 200 × 200 μm. The experimental conditions used allowed to work in transmission mode, allowing the beam to scan the welded joint starting from the BM, passing through the HAZ and fusion zone (FZ), until reaching the BM region on the other side. Consecutively analysis spots distanced 200 μm. A PerkinElmer 2D detector was utilized to capture the raw Debye-Scherrer rings. The acquired data was processed using a combination of Fit2D and MAUD (Material Analysis Using Diffraction) software to determine the existing phases in the welded joint and analyze their fraction evolution.

2.4. Thermodynamic calculations

In welded joints, accurate prediction of the non-equilibrium solidification path and phase structure evolution is of interest for gaining a comprehensive understanding of the microstructural formation and properties during the welding process. Thermo-Calc 2023a software provides a CALPHAD-based thermodynamic non-equilibrium solidification calculation method. To predict the solidification behavior under non-equilibrium conditions, the Scheil-Gulliver model was used. Aside from the phases that are expected to be formed, their stability domains and solidification temperature range can be captured. Scheil-Gulliver solidification simulations were carried out using the TCHEA5.1 thermodynamic database within the Thermo-Calc software. No kinetic databases (MOBNI or MOBHEA) were employed. Carbon (C) was set as a fast diffuser to account for its high diffusivity. The model also implicitly assumes an infinite cooling rate in the solid, although based on typical GMAW conditions, the estimated cooling rate in the fusion zone is approximately 10^3–10^4 °C/s. To account for potential variations in the solidification path of the material, the calculations employed using the average composition of the FZ as obtained by EDS measurements. The predicted phase structure is then compared to the synchrotron radiation data to unveil the role of both process thermal cycle and addition of the Inconel 625 filler material. This comparison serves two purposes. Firstly, it allows for the validation of the model's accuracy by assessing how well the predicted phase structure aligns with the experimental data. Secondly, it provides insights into areas where the model can be further improved to enhance its predictive capability for accurately capture non-equilibrium solidification paths and phase structure evolution in welded joints based on HEAs.

2.5. Microhardness and mechanical testing

To further investigate the influence of the weld thermal cycle on the micro and macro mechanical properties of the welded joints, microhardness characterization and uniaxial tensile testing were conducted. Microhardness measurements were performed using a Mitutoyo HM-112 microhardness testing machine, covering the entire crossing section and probing the BM, HAZ and FZ. During the measurement process, a load of 200 g was applied, and the distance between consecutive indentations was set to 200 μm, with a dwell time of 10 s for each indentation.

Uniaxial tensile tests were conducted using a Shimadzu tensile

Table 1
Presents the chemical composition of the raw materials, including the CoCrFeMnNi base material (BM) and Inconel 625 filler wire.

	Co	Cr	Mn	Fe	C	Nb	Mo	Ni
Base materials (at. %/wt. %)	**20.0/21.0**	**20.0/18.5**	**20.0/19.6**	**20.0/19.9**	**–/–**	**–/–**	**–/–**	**20.0/21.0**
Filler materials (at. %/wt. %)	**0/0**	**24.6/21.5**	**0.5/0.5**	**5.3/5.0**	**0.5/0.1**	**2.2/3.5**	**5.6/9.0**	**Balance**

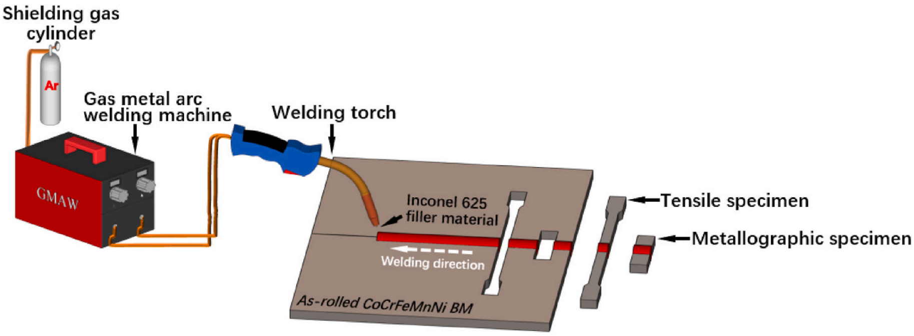

Fig. 1. Schematic representation of the experimental setup used for gas metal arc welding.

testing machine equipped with a 50 kN load cell, at room temperature. The loading direction was perpendicular to the welding direction, and the displacement rate was set to 1 mm/min. Digital image correlation (DIC) was employed during the tensile testing to evaluate the load partitioning in each typical welded region (BM, HAZ and FZ).

By utilizing microhardness measurements and uniaxial tensile tests, a comprehensive assessment of the mechanical response, at the micro and macro level, of the welded joint was achieved. This assessment allowed for an evaluation of the influence of the microstructural evolution on the mechanical properties within the joint.

2.6. *Strengthening calculations*

With the aim of further investigate the contributions of various strengthening mechanisms to the yield strength of the three regions (BM, HAZ, and FZ) of the welded joints, this study quantitatively evaluated the effects of grain boundary strengthening (σ_{HP}), dislocation strengthening (σ_{dis}), and solid solution strengthening (σ_{SS}). For welded joints of CoCrFeMnNi HEA fabricated by fusion-based welding, grain boundary strengthening, precipitation hardening strengthening and dislocation strengthening are considered as the primary strengthening mechanisms [15]. Considering the inherent nature of solid solution strengthening in HEAs, the overall estimated yield strength in this work can be expressed by:

$$\sigma_y = \sigma_{HP} + \sigma_{dis} + \sigma_{pre} + \sigma_{ss} \tag{2-1}$$

In equations (2)–(1), σ_y represents the yield strength of each region within the joint, which is obtained by extracting information from the stress-strain curves of these regions using DIC. σ_{dis} refers to the contribution of dislocation strengthening, while σ_{pre}, σ_{SS} and σ_{HP} represent the contribution of precipitation hardening strengthening, solid solution strengthening and grain boundary strengthening. Here, it is worth mentioning that σ_{pre} was assumed to be ≈ 0. Specifically, for the BM and HAZ, only a small fraction of Cr-Mn oxides was found, and these oxides are formed due to the contamination during cast of the original BM. For the FZ, the fast-cooling rate associated with the welding process restricts the time available for nucleation and growth of precipitates, limiting their overall impact in the yield stress. The detailed calculations for each strengthening are shown as below.

First, σ_{HP} characterizes the effect of grain boundary strengthening using the conventional Hall-Petch relation, which it can be expressed by Refs. [16,20]:

$$\sigma_{HP} = K \text{ x } d^{-1/2} \tag{2-2}$$

Here, K and d represent the Hall-Petch coefficients (494 MPa $\mu m^{1/2}$ [20]) and average grain size, respectively.

Next, the expression for dislocation strengthening, σ_{dis}, is given by the following equation:

$$\sigma_{dis} = M\alpha Gb\rho^{1/2} \tag{2–3}$$

In this equation, M represents the average Taylor factor, which was obtained from the EBSD data obtained in the current work; α i a constant (α ≈ 0.2 [21]); G is the shear modulus of the FCC matrix phase, approximately 76.9 GPa [22]; b is the length of the Burgers vector (b = 0.254 nm [21]); ρ is the dislocation density, and its calculation process using synchrotron X-ray diffraction data is detailed in Ref. [23].

In synchrotron X-ray diffraction analysis, the full width at half maximum (FWHM) of the diffraction peaks can be used to assess the variation in dislocation density. There are two main factors that primally influence the FWHM: grain size and defects. These two factors are the most influential causes for the ultimate variation in dislocation density. However, it is important to note that the variation in grain size does not directly affect the dislocation density from a materials science perspective. Therefore, in this study, the FWHM variations caused by changes in grain size (referred to as $FWHM_{size}$) are excluded, and only the FWHM variations attributed to internal microstrain within the material (referred to as $FWHM_{microstrain}$) are considered. This approach provides a more intuitive representation of the variation in dislocation density. The specific expression is given below [24] as:

$$FHWM = FWHM_{size} + FWHM_{microstrain} \tag{2–4}$$

$$FWHM_{size} = \frac{k\lambda}{L} \text{ x } \frac{1}{\cos\theta} \tag{2–5}$$

$$FWHM_{microstrain} = 4\varepsilon_0 \frac{\sin\theta}{\cos\theta} \tag{2–6}$$

By substituting equations (2)–(5) and (2–6) into equations (2)–(4), the resulting expression is:

$$FWHM \text{ x } \cos\theta = \frac{k\lambda}{L} + 4\varepsilon_0 \sin\theta \tag{2–7}$$

According to equations (2)–(7), FWHM x cosθ can be expressed as y, and 4sinθ can be expressed as x. Considering a linear equation of the y = m x + c type, where the intercept, c, corresponds to k x λ/L, and the slope, m, corresponds to ε_0. Therefore, by plotting the linear relationship between FWHM x cosθ and 4sinθ, the intercept c can be obtained. Substituting the obtained intercept into equations (2)–(5) allows for the calculation of $FWHM_{size}$. Furthermore, equations (2)–(6) can be view as a linear equation passing through the origin, y = m x *x*, where the slope m corresponds to the $FWHM_{microstrain}$ caused solely by internal defects such as microstrain. By performing a linear fit on $FWHM_{microstrain}$ and 4 sinθ/cosθ, the slope represents ε_0 caused solely by internal defects. Substituting this value into equations (2)–(8) yields the resulting dislocation density, ρ, caused by these factors.

$$\rho = \frac{k\varepsilon_0^2}{b^2} \tag{2–8}$$

Finally, the solid solution strengthening contribution (σ_{ss}) was modeled using Varvenne's model [25]. The yield stress of a solid solution at 0 K is determined by Equations (2)–(9), whereas the activation energy for the movement of dislocation is given by Equations 2–10.

$$\tau_{y0} = 0.051\alpha^{-\frac{1}{3}} G \left(\frac{1+\nu}{1-\nu}\right) f_1(w_c) \left(\frac{\sum_{i=1}^{n} c_i \Delta \overline{V}_i^2}{b^6}\right)^{\frac{2}{3}} \tag{2–9}$$

$$\Delta E_b = 0.274\alpha^{\frac{1}{3}} G b^3 \left(\frac{1+\nu}{1-\nu}\right)^{\frac{2}{3}} f_2(w_c) \left[\frac{\sum_{i=1}^{n} c_i \Delta \overline{V}_i^2}{b^6}\right]^{\frac{1}{3}} \tag{2-10}$$

where b is the modulus of the Burgers vector, G is the shear modulus and ν is the Poisson's ratio. Functions $f_1(w_c)$ and $f_2(w_c)$ are associated with the core structure of the dislocation, and their values are approximately constant, being 5.70 and 0.35 respectively. The terms c_i and ΔV_i represent the concentration of "solute" i and the volume mismatch caused by the presence of atom "i" in average matrix. The parameter α is a dimensionless constant related to the value of the dislocation line tension, which is given by $\Gamma = \alpha\mu b^2$. Atomistic simulations on several face-centered cubic (FCC) metals [26] indicate that $\alpha = 1/8$ serves as a good approximation in practice.

The yield stress correction, due to the thermal contribution and strain rate, is given by Equations 2–11 and (2-12) as shown below.

$$\sigma_{ss}(T,\dot{\varepsilon}) = M\tau_{y0} \exp\left(-\frac{1}{0.51}\frac{kT}{\Delta E_b}\ln\frac{\dot{\varepsilon}_0}{\dot{\varepsilon}}\right) \quad \frac{\sigma_{ss}}{M\tau_{ss,0}} \leq 0.5 \tag{2-11}$$

$$\sigma_{ss}(T,\dot{\varepsilon}) = M\tau_{y0} \left[1 - \left(\frac{kT}{\Delta E_b}\ln\frac{\dot{\varepsilon}_0}{\dot{\varepsilon}}\right)^{\frac{2}{3}}\right] \quad \frac{\sigma_{ss}}{M\tau_{ss,0}} \geq 0.5 \tag{2-12}$$

where M is the Taylor factor, k is the Boltzmann constant, T is the temperature, $\dot{\varepsilon_0}$ is the reference strain rate and $\dot{\varepsilon}$ is the experimental strain rate. Following Varvenne's model [25], $\dot{\varepsilon}_0$ was set as $10^4 s^{-1}$. In the range $0.3 \leq \tau_y/_{\tau_{y,0}} \leq 0.6$, Equations 2–11 and (2-12) yield very close results.

In the previous equations, the rule of mixtures ($\overline{V} = \sum_i c_i V_i$) was used to calculate the average atomic volume of the effective matrix. The latter parameter is related to the lattice parameter of an FCC structure by equation $\overline{V} = a^3/4$. The volume mismatch caused by each element in solution is given by $\Delta\overline{V}_i = V_i - \overline{V}$, where V_i is the apparent volume of the i-th element in the solid solution. The apparent atomic volume of each element utilized in this study is presented in Table 2 and was previously estimated in Ref. [26].

The elastic constants of base metal (CoCrFeMnNi) and Inconel 625 alloy used in the Varvenne's model are summarized in Table 3.

3. Results and discussion

3.1. Microstructure evolution

Fig. 2 a) illustrates the macroscopic morphology of the cross-section of the welded joint. No defects such as porosity or cracks were observed, suggesting a defect-free owing to the suitability of the selected process parameters. The boundary between the HAZ and FZ is delineated by white dashed lines. The visible reinforcements on the face and root of the joint are attributed to the filler wire utilized which provides excess material to the joint [30].

Table 2

Apparent atomic volume of elements in an FCC solid solution.

Element	Ni	Cr	Co	Fe	Mn	Mo[a]	Nb[b]
Atomic volume (Å^3) – this work	10.94	12.86	11.52	12.18	12.66	15.21	17.79

[a] Calculated in this work using the lattice parameter of Ni-Mo solid solution extracted from Ref. [27].

[b] Calculated in this work using the lattice parameter of Ni-Nb solid solution extracted from Ref. [28].

Table 3

Elastic constants of CoCrFeMnNi and Inconel 625 alloys used as input in Varvenne's model.

Alloy	Shear modulus [GPa]	Poisson ratio
CoCrFeMnNi	76.9	0.26
Inconel 625 [29]	78.0	0.31

Fig. 2 b1) to Fig. 2 b4) provide optical microstructure images of different regions of the welded joint, namely the BM, HAZ near the BM, HAZ near the FZ, and FZ, where distinct microstructural features can be observed. In the BM region, the grain size is relatively small due to the highly deformed grain structure that developed caused by the cold-rolling process. A noticeable grain growth can be observed from the low-temperature HAZ (refer to Fig. 2 b2)) to the high-temperature HAZ (refer to Fig. 2 b3)), which attributed to the effect of the weld thermal cycle. In the FZ, a typical columnar dendritic grain morphology is evident, which arises from the rapid melting and solidification processes in this region. Overall, the variations in microstructural and grain size among different regions of the welded joint are related to the weld thermal cycle, which will be further elucidated when considering the EBSD data.

To comprehensively extract more grain structure information and crystallographic features from the different regions throughout the whole welded joint, EBSD was performed. EBSD is an effective microstructural characterization technique for microstructure analysis, which can provide structure information, including grain orientation and sizes, grain boundary distributions, and crystal defects, for example.

Fig. 3 a) details the EBSD map of the joint cross-section, complementing the macroscopic morphology depicted in the optical microscope image of in Fig. 2 a). This confirms once again that the welded joint obtained in the current work is defect-free and fully penetrated, showcasing the successful metallurgical bonding between the CoCrFeMnNi HEA and the Inconel 625 filler wire using arc-based processes. The black dashed lines represent the boundary between the HAZ and the FZ, which were determined based on the differences in the microstructural characteristics observed in these locations, as highlighted in Fig. 3 b2) and b3).

The BM, HAZ near the BM, HAZ near the FZ, FZ near the HAZ/FZ boundary and the center of the FZ, exhibited different microstructural characteristics. For the BM, which has been previously discussed [31, 32], the microstructure undergoes approximately ≈ 50 % cold rolling prior to welding. This results in elongated grains along the rolling direction, forming a pancake-like structure with a grain width ranging between 2 and 3 μm. Such microstructure features are commonly observed in the cold-rolled CoCrFeMnNi HEA. Following, focus will be on the microstructure changes induced by the weld thermal cycle in other regions of the welded joint.

The HAZ near the BM region (refer to Fig. 3 b1)), is defined in this work as the low-temperature HAZ, denoted as HAZ1. It is formed as a result of the welding process, undergoing what could resemble a short and low-temperature heat treatment. From the Inverse Pole Figure (IPF) map of this region (refer to Fig. 3 b1)), a significant presence of fine equiaxed grains can be observed, evidencing the occurrence of recrystallization. Additionally, a large number of Σ3 annealing twins are observed within the recrystallized grains (refer to Fig. 3 c)), revealing that the weld thermal cycle near HAZ1 can induce the formation of these annealing twins in the previously cold-rolled BM. Moreover, most of the recrystallized grains are interconnected by high-angle grain boundaries (HAGBs), forming a network, as indicated by the bright red solid lines in Fig. 3 c1). Furthermore, a slight increase in grain size was observed, with the average grain size increasing from 2 to 3 μm (BM) to ≈ 4.5 μm (refer

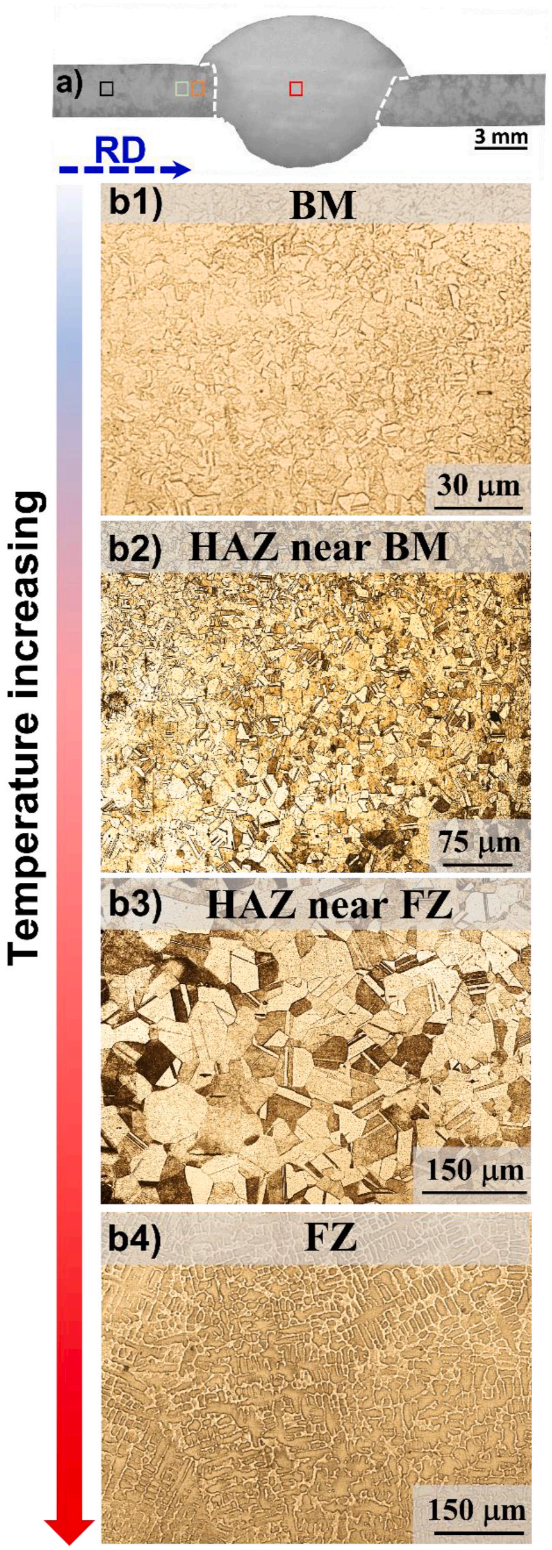

Fig. 2. Light optical microscopy of the gas metal arc welded CoCrFeMnNi joint obtained with Inconel 625 filler wire: a): overview of the joint cross section; representative micrographs of: b1): BM; b2): HAZ near the BM; b3): HAZ near the FZ; b4): FZ.

to Fig. 3 e)). It is important to note that the original BM, which was subjected to extensive cold deformation, contains almost no $\Sigma3$ annealing twins. This is attributed to the fact that the BM microstructure preserves its heavily deformed state and is not affected by the weld thermal cycle.

The next region, corresponding to the HAZ near the FZ, is defined as the high temperature HAZ, designated as HAZ2, which can be interpreted as a region that experiences a high temperature annealing-like heat treatment during welding. Within HAZ2, the grain size becomes significantly coarser (refer to Fig. 3 b2)), with the average grain size increasing from $\approx$4.5 μm (HAZ1) to $\approx$ 14.3 μm (HAZ2) (refer to Fig. 3 e)). This difference in grain size within the HAZ can be explained by the weld thermal cycle. Specifically, the peak temperature and the duration at high temperatures progressively diminish towards the BM. Near the HAZ2, both the peak temperature and the temperature duration for grain growth to occur are higher and longer compared to those near HAZ1. Therefore, the grain growth mechanism is more pronounced in HAZ2 compared to the recrystallization mechanism in HAZ1. The number of $\Sigma3$ annealed twins show a decreasing trend in this region (refer to Fig. 3 c2)), which is related to the grain growth process. Specifically, grain growth involves the migration of grain boundaries and twin boundaries, and the rapid migration of these boundaries can collide with other boundaries, leading to the consumption of twin boundaries. Twin boundaries are the interfaces that exist within the grains, and their depletion leads to a reduction in the number of annealed twins. In other words, $\Sigma3$ annealed twins gradually disappear during the grain growth through the migration of grain boundaries and twin boundaries [33]. Similarly, the HAGB in the region decreases accordingly (refer to Fig. 3 c3)), which is due to the combined effects of grain boundary adjustments and grain size enlargement during grain growth and grain boundary migration.

Based on the above analysis, it is evident that significant effect to the solid-state phase transformations throughout the whole HAZ, encompassing both HAZ1 and HAZ2. These transformations include recovery, recrystallization and grain growth. The occurrence of these phenomena is influenced the pre-existing strain energy stored in the BM, upon which the process thermal cycle will allow the activation of thermally active, solid-state processes. Higher temperatures and longer durations at peak temperatures facilitate grain boundary migration and adjustment, as well as grain growth. These conditions promote the coarsening and enlargement of grains within the HAZ. On the other hand, the low/high temperature annealing-like heat treatments play a crucial role in releasing the stored strain energy present in the BM. This phenomenon is supported by the results obtained from the EBSD Kernel Average Misorientation (KAM) analysis (see Fig. 3d)). The release of strain energy is initiated by the weld thermal cycle and further contributes to the development of solid-state phase transformations within the HAZ.

Upon evaluating the FZ, completely different microstructural features can be observed in this region. In the FZ (refer to Fig. 3a)), large-sized ($\approx$351.12 μm) highly oriented grains are observed. Considering the limited number of grains included in the statistical analysis of KAM values and grain size in the center and edge regions of the FZ, which may affect the representativeness and reliability of the statistical results, the grain size statistics in this study were performed based on the entire FZ region. These grains grow epitaxially from the solidified FZ, exhibiting a preferential growth orientation along the (001) direction on the left side near the HAZ/FZ boundary (Supplementary Material, Fig. 1). In contrast, no distinct preferential orientation is observed at the center of the FZ or near the right side of the HAZ/FZ boundary, where the overall texture appears relatively random. It should be noted that grains on the left side of the FZ predominantly exhibit a <001> preferred orientation (refer to Supplementary Material, Fig. 1), whereas those on the right side tend toward a random orientation distribution. The formation of this orientation difference is influenced not only by the coupling relationship between the thermal gradient (G) and solidification rate (R) but also closely related to the crystallographic preferred growth direction, interfacial energy anisotropy, and the complex thermal-fluid coupling behavior within the molten pool. During the welding process, asymmetries in the molten pool morphology, heat source distribution, and the characteristics of the twin-wire arc input can all contribute to the

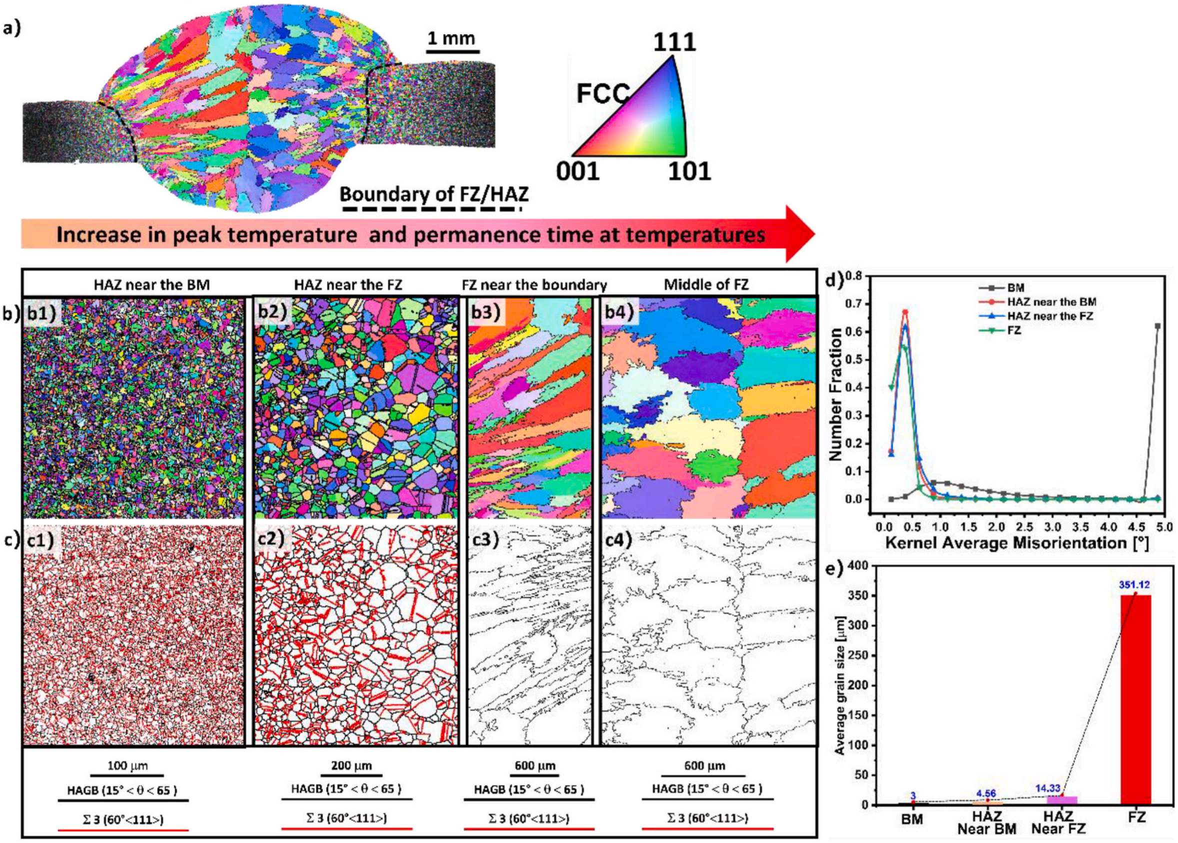

Fig. 3. A): EBSD map of the gas metal arc welded CoCrFeMnNi high entropy alloy with Inconel 625 filler wire; b1) – b4) and c1) – c4): IPF and Σ3 boundaries map of the HAZ near the BM, HAZ near the FZ, FZ near the boundary of the HAZ/FZ and middle of FZ, respectively; d) and e): variation of KAM and average grain size values with respect to the different regions of the joint, respectively.

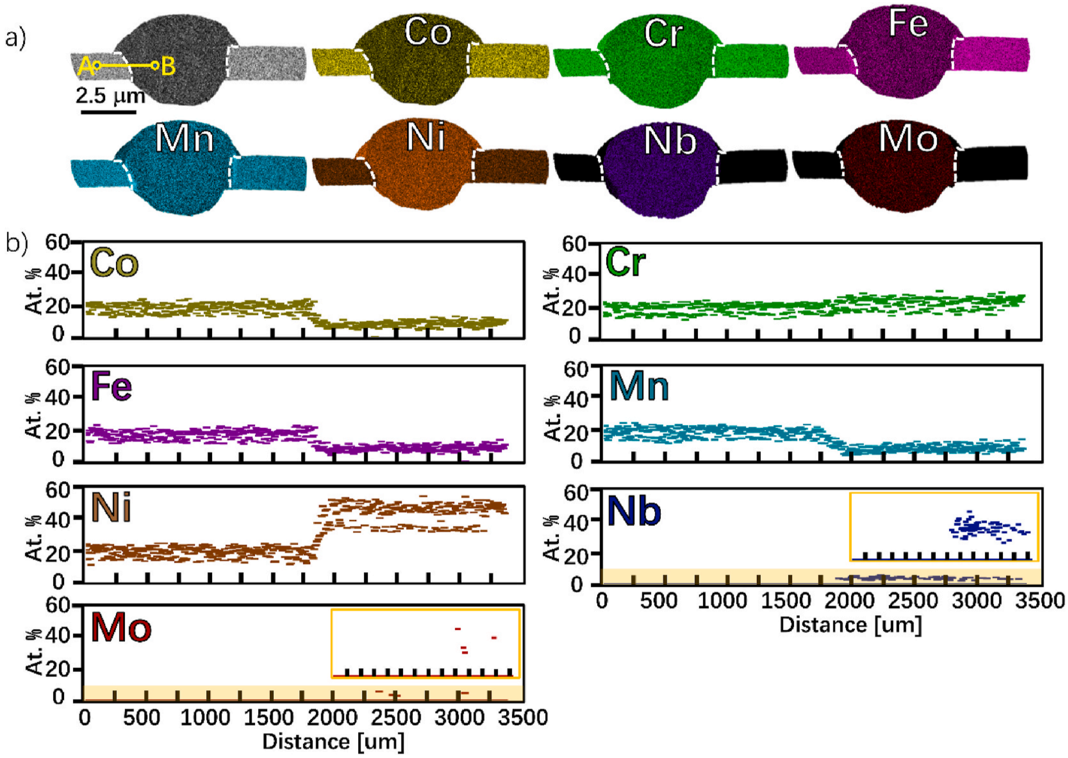

Fig. 4. A): EDS mapping of across the welded joint; b): EDS line scan along the yellow line of Fig. 4 a). (For interpretation of the references to color in this figure legend, the reader is referred to the Web version of this article.)

development of asymmetric thermal and flow fields on either side of the molten pool, thereby inducing different grain growth advantages in different regions. On the left side, the heat flow direction is more closely aligned with the <001> crystal growth direction, promoting the competitive growth and dominance of <001>-oriented grains. In contrast, on the right side, disturbances in heat flow or changes in cooling conditions weaken the preferential growth advantage, leading to a more randomized orientation distribution overall. Moving towards the central region of the FZ, large columnar grains, oriented perpendicular to the FZ boundary, can be observed growing towards the weld centerline. This type of growth behavior is influenced by the G and the R. The complete melting and rapid solidification experienced in the FZ leads to the loss of any previous thermomechanical processing of the BM, resulting in a microstructure resembling that of as-cast materials. Consequently, within this process, the presence of Σ3 annealed twins that formed in the HAZ are eliminated (refer to Fig. 3 c3) and c4)), and the HAGBs are uniformly distributed (refer to Fig. 3 c3) and c4)). It should be mentioned that the development of such a coarse grain structure is a common phenomenon during welding of this material [33]. It should be mentioned that due to the current limitations of EBSD in terms of scanning resolution, magnification, as well as the limited scanning area, the identification of nanoscale precipitates present in different regions of the joint is not possible. Therefore, the EBSD data provided here is solely used to identify the major microstructural features across the joint. However, the limitations of EBSD analysis resulting from these constraints will be addressed in detail through the use of synchrotron radiation analysis.

The EDS mapping of the entire welded joint (refer to Fig. 4 a)) reveals a relatively homogeneous distribution of elements. This indicates the formation of a reliable metallurgical blend between the CoCrFeMnNi HEA, serving as the BM, and the Inconel 625 filler wire, implying that these two materials can achieve good bonding and compatibility between them during the welding process. The formation of such metallurgical blend is expected to contribute to the enhancement of the strength and overall performance of these joints.

To further provide a clearer representation of the main composition changes (Co, Cr, Fe, Mn, Ni, Nb, and Mo) near the boundaries of the HAZ and FZ, an EDS line scan was conducted. The yellow solid line in Fig. 4 a) indicates the position of the line scan, while the white dashed line represents the boundary between the HAZ and FZ. The line scan results reveal that there is a redistribution of elements after entering the FZ, which is a typical characteristic associated with solidification in fusion-based welding processes. However, overall, the CoCrFeMnNi HEA and Inconel 625 are well mixed, and no macroscopic element segregation is observed. This effective mixing is attributed to the high cooling rate during the welding process, which limits the time available for macroscopic element segregation to occur. It is important to note that the presence of trace amounts of Nb and Mo elements observed in the FZ is related to the addition of the Inconel 625 filler wire. An interesting finding in this study is that the Mo content in the FZ is significantly lower than that of Nb in the EDS line scan analysis (refer to Fig. 4 b)), despite the fact that the Mo atomic percentage in the Inconel 625 filler wire (≈5.6 at. %) is higher than that of Nb (≈2.2 at. %). This phenomenon can be primarily attributed to the combined effects of elemental segregation during welding, the enrichment of secondary phases, and the localized nature of EDS detection. Specifically, due to the differences in the local temperature fields during welding, Mo and Nb exhibit significantly different solidification behaviors in the FZ, resulting in a lower enrichment of Mo compared to Nb in this region. Additionally, the spatial resolution of the EDS line scan analysis may affect the accuracy of elemental signals, further amplifying the observed low Mo content. This phenomenon aligns with the general behavior of elemental segregation during dissimilar welding of HEAs and nickel-based alloys, revealing the solidification behavior and interactions of different elements during the welding process.

To provide a more illustrative depiction of the microstructural evolution across the welded joint where no melting occurs, Fig. 5 presents the corresponding schematic diagram. The initial microstructure exhibits a pancake-like morphology with a high density of dislocations and deformed twins (refer to Fig. 5a)). Upon entering the low temperature HAZ, the pre-existing stored strain energy is released, resulting to the occurrence of recovery (refer to Fig. 5b)) and subsequent recrystallization. This recrystallization process leads to the formation of fine equiaxed grains (refer to Fig. 5c)). Further moving closer to the heat source into the high temperature HAZ, grain boundaries and twin boundaries start to migrate and consume each other (refer to Fig. 5d)), leading to the phenomenon of grain coarsening. Eventually, in the FZ (refer to Fig. 5e), complete melting and rapid solidification leads to the formation of coarser, preferentially oriented grains with dendritic structures along the grain boundaries.

Fig. 6 a) depicts the superimposed synchrotron diffraction patterns obtained from scanning the entire welded joint. The different regions of the joint, BM, HAZ1, HAZ2, and FZ, can be distinguished based on the maximum intensity variations of the diffraction peaks. These regions are denoted by color red, pink, blue, and yellow, respectively, with boundary lines delimitating them. To gain a better understanding on the influence of the weld thermal cycle on the microstructural features of these different regions, Fig. 6 b) to e) provide the phase identification results obtained from representative diffraction patterns for each region. These diffraction patterns are utilized to extract crystallographic information from each region, including phase structure, phase volume fraction, space group, and lattice parameters. The volume fractions of each phase structure obtained through Rietveld refinement method are detailed in the pie chart of Fig. 6 e).

Based on the phase identification results, it can be observed that the BM, HAZ1, and HAZ2 all possess the same matrix phase, corresponding to an FCC structure. In addition, there is a small amount of Cr-Mn-based oxides observed, which correspond to low-intensity diffraction peaks. The presence of these oxides is mainly attributed to potential contamination in the raw materials and oxidation reactions during the manufacturing process [34]. According to the Rietveld refinement results (refer to Fig. 6 f)), the volume fraction of these Cr-Mn oxides is very low. They account for approximately ≈1.25 % in the BM, ≈1.31 % in HAZ1, and ≈1.83 % in HAZ2. Although there is a slight increasing trend in the volume fraction of these oxides, they do not affect the mechanical properties of the material [35].

Upon entering the FZ (refer to Fig. 6 e)), a significant change in the microstructure is observed. In addition to the previously identified FCC matrix phase (≈94.29 %) and Cr-Mn oxides (≈2.39 %), the presence of Nb-rich carbides (≈0.79 %), Laves (≈0.87 %), γ (≈0.49 %), and σ phases (≈1.17 %) is detected. The existence of these four phases is primarily attributed to the compositional changes induced by the addition of the Inconel 625 filler wire in the FZ. According to previous literature investigation, Li et al. [36] and Hu et al. [37] have separately introduced Nb and Mo into CoCrFeMnNi HEA and found that these two have the propensity to promote the formation of Laves and σ phases, respectively. Therefore, the addition of the Inconel 625 filler wire during welding can be considered as the primary cause for the formation of Laves and σ phases in the FZ. Furthermore, it is known that Nb element, made available in the FZ upon melting of the filler wire, has a strong affinity with carbon and is prone to forming Nb-rich carbides [38], which thus justifies the presence of this phase in the FZ. Moreover, the thermodynamic calculations confirmed that the precipitation of the NbC phase occurs not only during the initial solidification process from the liquid state (refer to Fig. 7) but also continuously during subsequent cooling process from approximately 1228 °C–659 °C (refer to supplementary material, Fig. 2). These findings further support the experimental detection of Nb-rich carbides in the FZ.

The lattice parameters of the phase structures present in each region of the welded joint are summarized in Table 4. Here, particular attention is given to the lattice parameter variations of the FCC matrix phase. The matrix phase FCC in the rolling state of the BM region, possesses a lattice

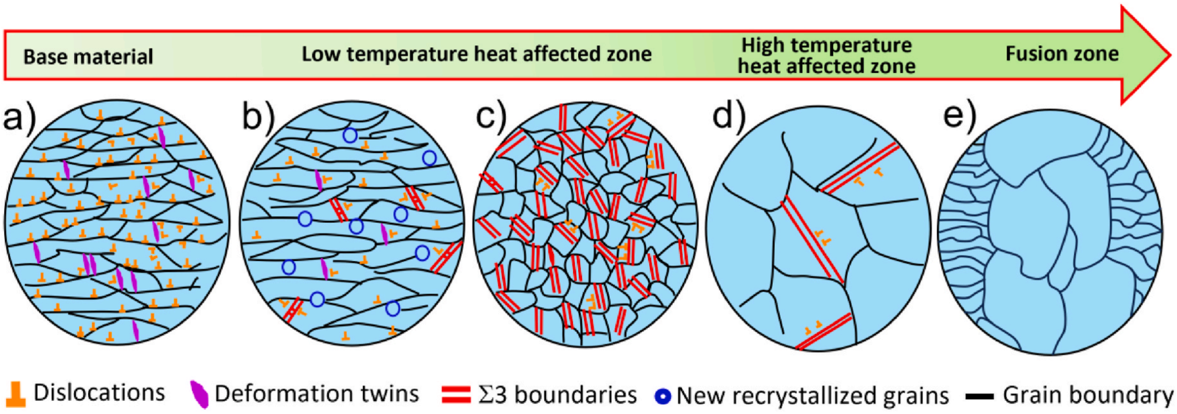

Fig. 5. Schematic illustration of microstructure evolution induced by the weld thermal cycle effect on the rolled base material (from left to right): a) initial rolled base material; b) HAZ subjected to low temperature; c) – d) HAZ subjected to high temperature and e) FZ.

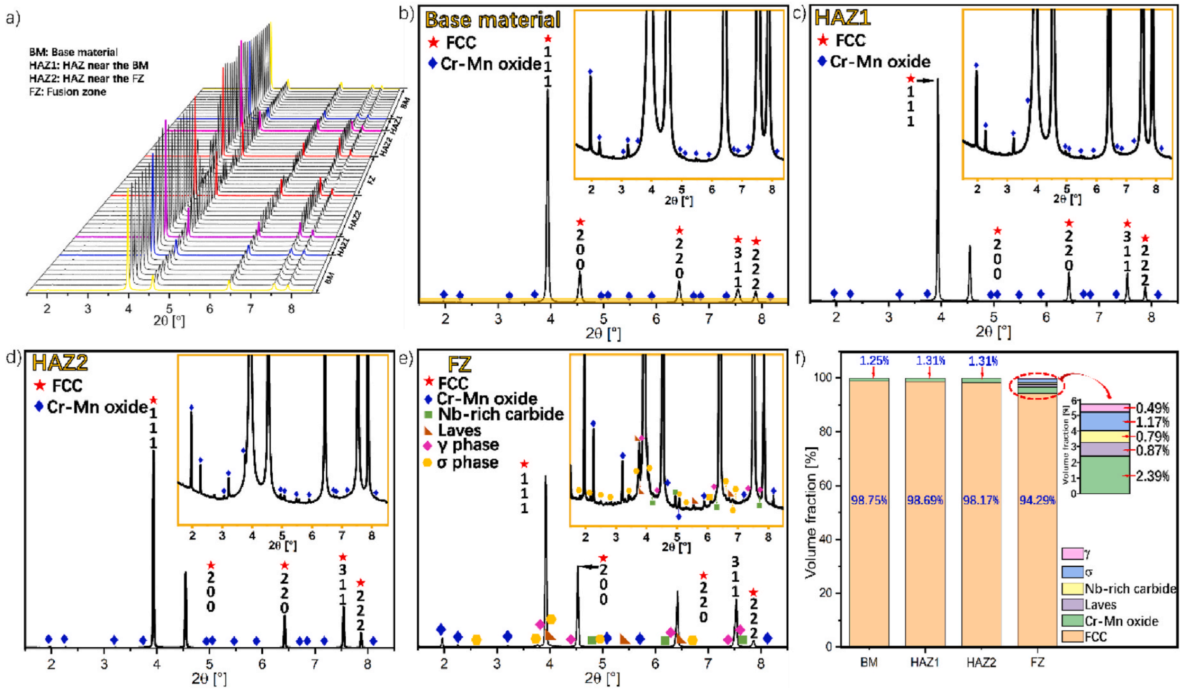

Figs. 6. 3D plot and phase identification of existing phases within the welded joint using high energy synchrotron X-ray diffraction: a): Superimposition of different patterns across the welded joint; b), c), d) and e) are representative diffraction patterns from the BM, HAZ near the BM, HAZ near the FZ and FZ, respectively; The inserts in b), c), d) and e) highlight the presence of trace amount of precipitates and secondary phases. f): Volume fraction evolution of the existed phases across the welded joint (BM, HAZ1, HAZ2 and FZ) as obtained by Rietveld refinement.

parameter of approximately ≈3.5872 Å. Upon entering the HAZ, a slight change in the lattice parameter is observed, with HAZ1 and HAZ2 corresponding to lattice parameters of about ≈3.5877 Å and ≈3.5885 Å, respectively. This change is primarily attributed to lattice thermal expansion caused by the weld thermal cycle and the release of pre-existing strain energy stored in the BM region. In the FZ, the lattice parameter of the FCC matrix phase increases to approximately ≈3.5897 Å. There are two possible reasons for this variation: one is that the addition of Nb and Mo elements from the Inconel 625 filler wire have larger radii compared to other elements in the FZ, which can lead to lattice distortion and an increase in the lattice parameter [39, 40]; the second one is that the rapid heating and solidification during the welding process can cause residual stresses in the FZ, which can also lead to a slight variations in the lattice parameter. Nonetheless, given the magnitude of the changes in the lattice parameter of the FZ it is expected that the major drives for this to occur is by the addition of both Nb and Mo, rather than from the welding residual stresses.

To better understand the non-equilibrium solidification experienced in the FZ, the Scheil-Gulliver model, available in ThermoCalc, was utilized to predict the solidification path and phase structures that are expected to be formed in this region. Here, considering the non-equilibrium conditions during solidification of the FZ, there is elemental redistribution and certain low melting elements, namely as Mn, can preferentially evaporate, thereby altering causing changes in the nominal composition of the alloy. Therefore, in the current work, the Scheil-Gulliver model was applied using the average composition of the FZ (44.3 % Ni, 24 % Cr, 9.3 % Fe, 9.2 % Co, 8.9 % Mn, 2.9 % Mo, 1.3 % Nb and 0.1 % C, at. %), which was determined through EDS measurements. During calculations, C was set as a fast diffuser.

According to the thermodynamic simulations using the Scheil-Gulliver model (refer to Fig. 7), the solidification process begins at 1377.91 °C (liquidus temperature) and initially forms the FCC matrix

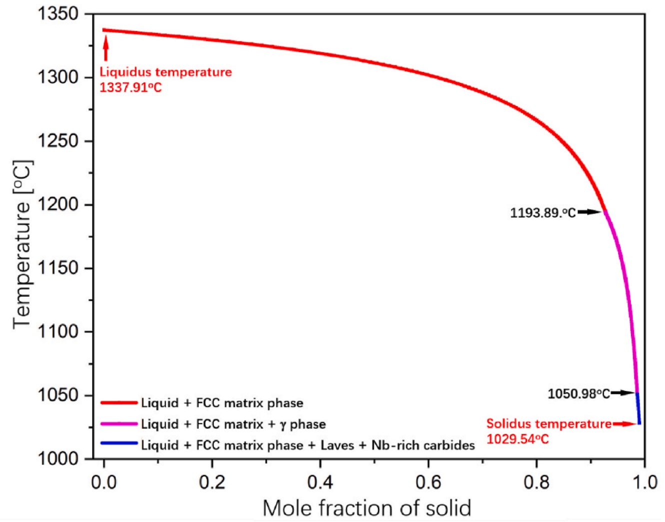

Fig. 7. Solidification path calculations using the Scheil-Gulliver model in ThermoCalc (TCHEA 5.1 database) considering the average composition of the fusion zone.

Table 4
– Refined lattice parameters from the BM, HAZ near the BM (HAZ1), HAZ near the FZ (HAZ2) and FZ.

	FCC	Cr-Mn oxide	Laves	Nb-rich carbide	σ phase	γ phase
	Fm-3m	Fm-3m	P63/mnm	Fm-3m	$P4_2$/mnm	Fm-3m
BM	a ≈3.5872 Å	a ≈7.5619 Å	–	–	–	–
HAZ1	a ≈3.5877 Å	a ≈7.5699 Å	–	–	–	–
HAZ2	a ≈3.5885 Å	a ≈7.5695 Å	–	–	–	–
FZ	a ≈3.5897 Å	a ≈7.5673 Å	a ≈ b ≈ 2.4804 Å	a ≈3.43 Å	a ≈ b ≈ 8.80 Å α = β = γ = 90°	a ≈2.36 Å

phase (Liquid → Liquid + FCC matrix phase) within the temperature range between 1377.91 and 1193.89 °C. In the subsequent reactions, the liquid phase gradually transforms into a mixture of Liquid + FCC matrix phase + γ phase. Finally, the remaining liquid solidifies to form FCC, Laves phase, and Nb-rich carbides (Liquid → Liquid + FCC matrix phase + Laves + Nb-rich carbides), terminating the solidification at 1275 °C (solidus temperature). The predictions of the Scheil-Gulliver model indicate that the solidification process in the FZ involves one matrix phase (FCC) and three precipitated phases (γ phase, Nb-rich carbides and Laves phase), which is consistent with the phase identification performed through synchrotron radiation experiments (refer to Fig. 6 e)), and these phases (matrix FCC phase, γ phase, Laves phase, and Nb-rich carbides) are directly formed from the liquid during solidification. However, the synchrotron radiation experiments also detected the presence of Cr-Mn oxides and σ phase in the FZ, which were not anticipated by the Scheil-Gulliver model. Regarding Cr-Mn oxides, their absence in the model's predictions can be explained considering that their formation is mainly derived from potential contamination in the raw materials and oxidation reactions induced by the high temperatures experienced in the FZ, rather than being a result of metallurgical solidification reactions of the alloy system used in this work. Additionally, the lack of σ phase in the model's predictions suggests that the observed σ phase in the FZ (refer to Fig. 6 e)) may precipitates during the solid-state cooling (approximately ≈ 400 °C), as its formation is suppressed at high temperatures due to the rapid solidification and cooling rates experienced during welding. Here, it is important to clarify that although the cooling during welding is not "infinitely fast," solidification in the actual weld pool occurs under extremely rapid and non-equilibrium conditions. The Scheil-Gulliver model, despite its idealized assumptions (no diffusion in the solid phase and complete mixing in the liquid phase), provides a good approximation for simulating element partitioning and phase evolution under rapid solidification. In this study, the phases predicted by the model (FCC, Laves, NbC) show high consistency with experimental results from synchrotron radiation and EDS analysis, indicating that the predictions are reliable despite the simplified assumptions. Moreover, for multi-principal element high-entropy systems, there is currently a lack of accurate kinetic diffusion data (such as interdiffusion coefficients at high temperatures). Even when using kinetic models like DICTRA, significant errors may be introduced. Therefore, at this stage, the Scheil-Gulliver model represents a more practical and reasonable choice.

To further investigate the enriched components of the precipitated phases predicted in the FZ, compositional analysis of the dispersed, fine particles in this region was performed using EDS, as shown in Fig. 8. The EDS analysis revealed that three types of precipitated phases were detected: MC carbides (refer to Fig. 8 a)), Laves phase (refer to Fig. 8 b)), and Cr-Mn oxides (refer to Fig. 8 c)). Specifically, the detected MC carbides were found to be enriched in Nb and a small amount of Mo due to the strong affinity of Nb and Mo with C [41]. The detected Laves phase is also enriched with Nb and a small amount of Mo, though C-free. The formation of this phase can be attributed to two reasons: i) the presence of Nb itself can promote the formation of the Laves phase [42,43]; ii) during the final solidification stage, the Nb and Mo experience microscopic segregation, which ultimately leads to the formation of Laves phase [44,45]. It should be noted that the other two precipitated phases, γ and σ phase, were not detected due to the limitations of EDS analysis and the small size of these nanoscale phases.

3.2. Mechanical properties

To further explore the influence of microstructural evolution on the local mechanical properties of the welded joint, microhardness analysis was conducted across the welded joint, as shown in Fig. 9. The color variation observed in the microhardness mapping (refer to Fig. 9 a)) enables distinct identification of the various regions within the joint. Specifically, the color changes from red, to yellow, green, and blue, correspond to the BM, HAZ1 and HAZ2 and FZ, respectively.

To further reproduce more visually the variations in hardness among different regions of the welded joint, a microhardness line distribution was plotted along the half-thickness of the welded joint (refer to the white dashed line in Fig. 9 a)), as shown in Fig. 9 b). The different regions of the welded joint exhibit distinct hardness values due to the previously reported variations in microstructure. The BM region in the as-rolled condition exhibits a hardness value of approximately ≈400 HV0.5, into the HAZ (HA1 and HAZ2), the hardness values gradually decrease to about ≈150 HV0.5, which can be attributed to the release of the previously stored strain energy in the BM caused by the weld thermal cycles (refer to Fig. 3 d)), as well as the recrystallization and grain growth (refer to Fig. 3 c1)-c2) and e)).

Interestingly, the FZ with the addition of the Inconel 625 filler wire exhibits a noticeable increase in hardness, from approximately ≈150 HV0.5 to around ≈180 HV0.5. In contrast, the hardness changes in the FZ caused by using other filler wires, such as 410 martensitic stainless steel [46] and austenitic 308LSi stainless steel [31], are not as pronounced. This suggests that the addition of Inconel 625 wire induces a solid solution strengthening effect by altering the chemical composition of the FZ. Indeed, Inconel 625 itself is a nickel-based high-temperature alloy well known for its solid-solution strengthening effect [47], which

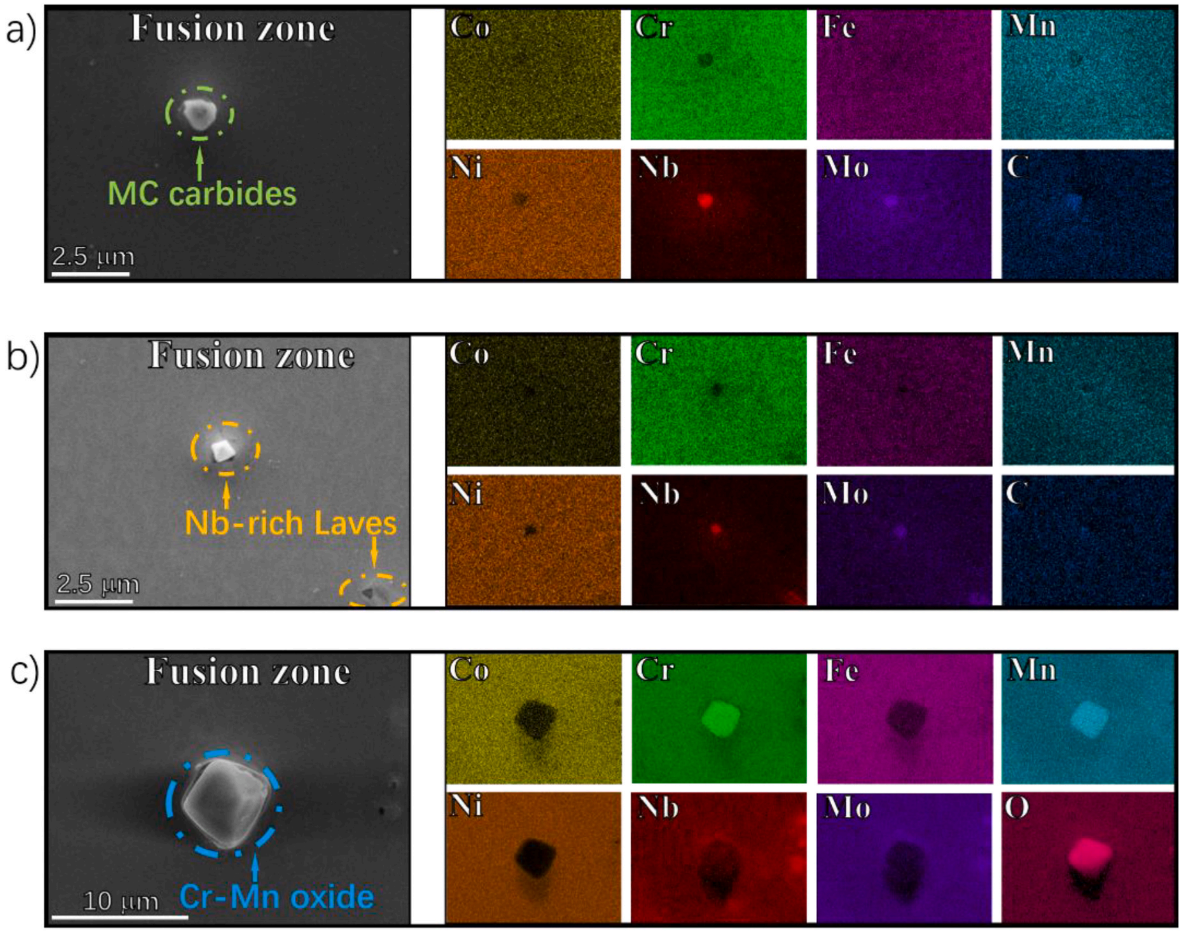

Fig. 8. SEM image and corresponding EDS mapping of a): MC carbides; b): Nb-rich Laves and c): Cr-Mn oxide in the fusion zone.

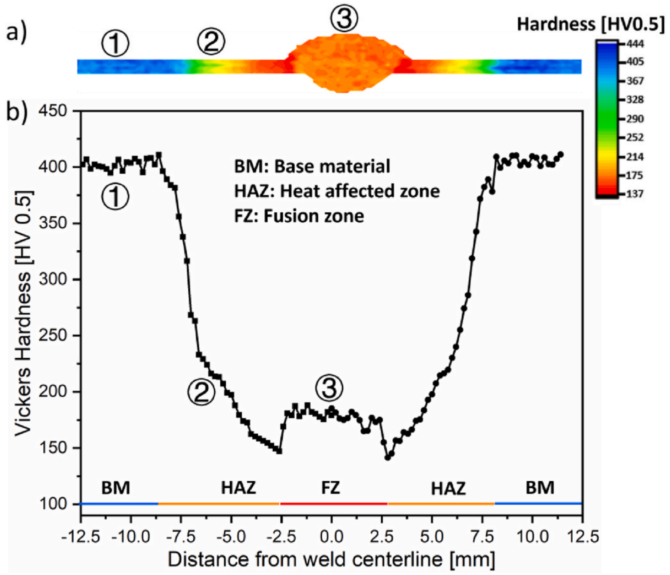

Fig. 9. A): Microhardness mapping over the welded joint; b): Microhardness distribution obtained along the mid height of the welded joint.

explains the observed hardness increase in the FZ. Overall, this solid solution strengthening effect has a positive impact on the local mechanical properties of the welded joint, since it can counterbalance the low hardness found in autogenous or heterogenous CoCrFeMnNi HEA welded using fusion methods.

To investigate the influence of adding Inconel 625 filler wire on the macroscopic mechanical response of the CoCrFeMnNi welded joints, tensile tests were performed. These results are depicted in Fig. 10,

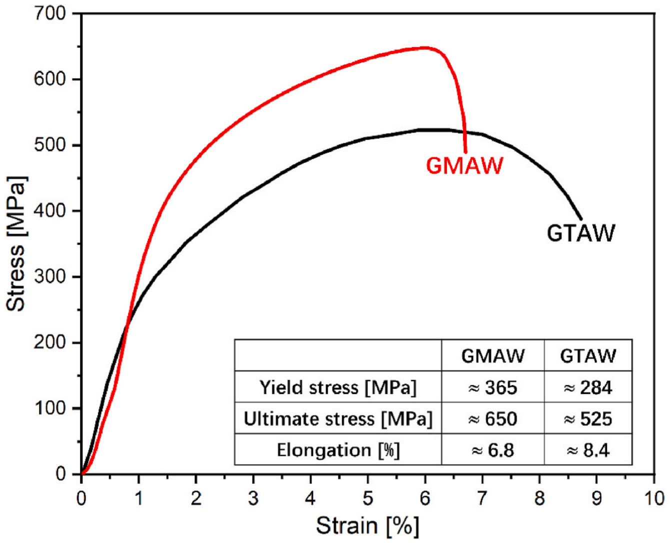

	GMAW	GTAW
Yield stress [MPa]	≈ 365	≈ 284
Ultimate stress [MPa]	≈ 650	≈ 525
Elongation [%]	≈ 6.8	≈ 8.4

Fig. 10. Tensile behavior comparison between a gas tungsten arc welded CoCrFeMnNi (obtained from Ref. [32]) and the present gas metal arc welded CoCrFeMnNi with Inconel 625 filler material. The inserted table details a summary of the tensile properties of both welded joints.

showcasing two conditions: with and without the addiction of filler wire. The solid red and black lines represent the stress-strain curves of the joints with and without the addition of filler wire, respectively. A table inserted in Fig. 10 summarizes the key mechanical properties of these two joints, including yield and tensile strength, and ductility.

Overall, the welded joint with the addition of filler wire (red line) exhibits superior yield strength (≈365 MPa vs. ≈ 284 MPa) and ultimate tensile strength (≈650 MPa vs. ≈ 525 MPa) compared to the joint without filler wire (black line). However, it shows slightly lower ductility (≈6.8 % vs. ≈ 8.4 %) than the joint without filler wire. Through microstructure analysis of the FZ, three main factors can explain the slightly improved in both yield strength and ultimate strength of the welded joint with filler wire. First, the addition of filler wire increases the cross-sectional area of the FZ, resulting in additional face and root reinforcements (refer to Fig. 2 a)), thereby enhancing its load-bearing capacity. Second, the Inconel 625, as a solid solution strengthening high-temperature alloy, contains Nb and Mo elements with larger atomic radii. These elements induce lattice distortion in the FZ, contributing to solid solution strengthening. Third, the precipitated phases induced by the addition of filler wire in the FZ may also contribute to this strengthening effect. Literature studies have shown that the introduction of Nb in CoCrFeMnNi HEAs results in the formation of Laves phases, which enhances the material strength [36]. Nb-rich carbides are typically distributed around grain boundaries, where they serve as dislocation pinning sites that hinder dislocation motion. This leads to an increase in dislocation density, enhances the dislocation strengthening effect, and ultimately improves the alloy's strength [38]. However, failure occurs at the interface between the HAZ and the FZ (at the weld toe), which can explain why the welded joint with filler wire exhibits slightly lower ductility compared to the joint without filler wire. The main reasons are twofold: i) the presence of face and root reinforcements at the weld toe leads to geometric defects, promoting crack initiation and facilitating stress concentration, ultimately leading to cracking; and ii) the presence of Nb-rich carbides and Laves phases increases the potential for hot cracking sensitivity [48,49], which can be detrimental to mechanical properties due to the potential formation of cracks during solidification. However, it should be noted that although the presence of Nb-rich carbides and Laves phases may increase the hot cracking susceptibility of the alloy system, no obvious cracking defects were observed in this study through optical and electron microscopy. Therefore, the reduction in ductility of the current welded joint is primarily attributed to the stress concentration effects at the weld toe and the local embrittlement induced by hard and brittle secondary phases, such as Nb-rich carbides, Laves phases, and σ phases, rather than by hot cracking. In addition, it is necessary to clarify the effect of the slight misalignment between the two sides of the BMs in the welded joint on the mechanical properties (Fig. 2a). Although slight misalignment between the base materials after welding was observed, which could introduce some shear components under uniaxial tensile loading, its influence on the mechanical behavior is considered limited in this study. The misalignment mainly arises from the formation of weld reinforcements caused by filler metal addition. To mitigate this in future work, optimization of welding parameters, post-weld machining to remove excessive reinforcements, and modified joint designs with pre-weld grooves will be considered. Furthermore, DIC analysis (Fig. 11a) indicated that fracture consistently initiated at the weld toe rather than in the fusion zone, suggesting that the primary tensile failure behavior was not significantly altered by the potential shear effects introduced by misalignment.

To further investigate the local mechanical response of different regions (BM, HAZ, welded toe, and FZ) within the welded joint, digital image snapshots taken at different loading stages (elastic, yielding,

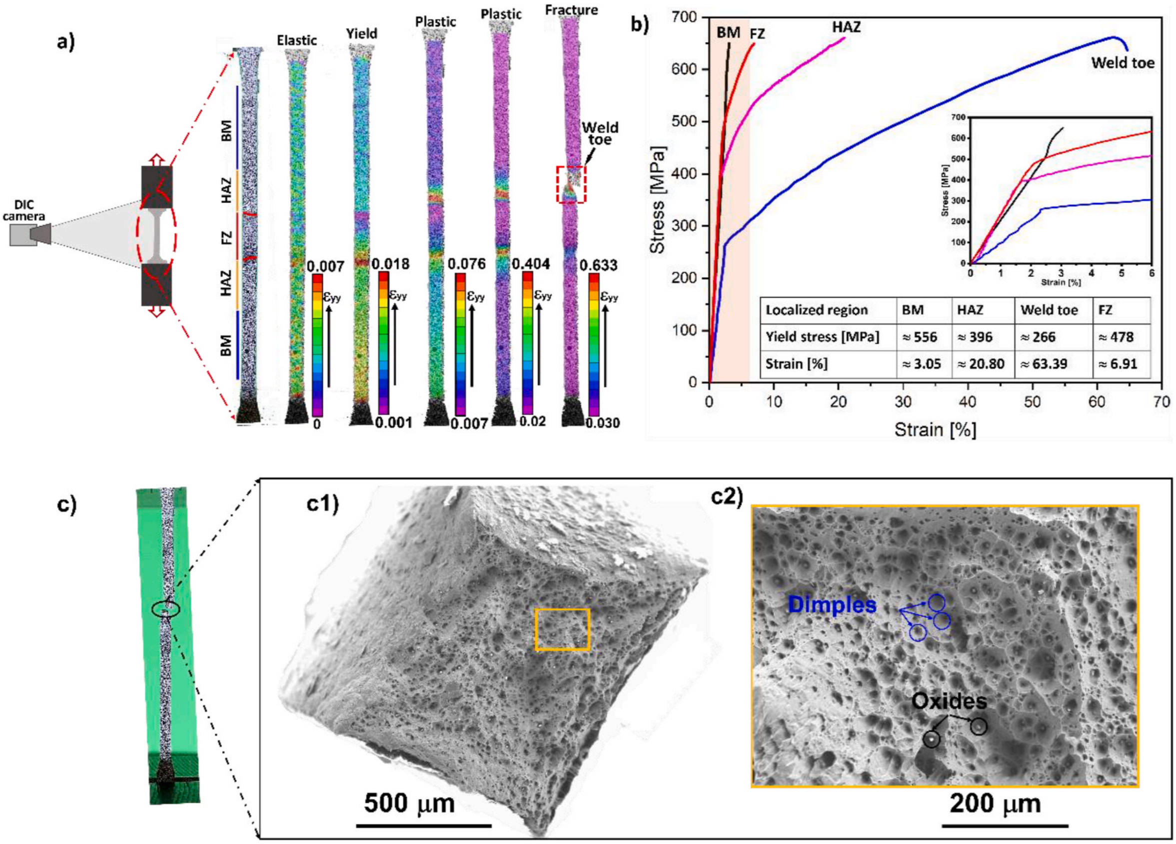

Localized region	BM	HAZ	Weld toe	FZ
Yield stress [MPa]	≈ 556	≈ 396	≈ 266	≈ 478
Strain [%]	≈ 3.05	≈ 20.80	≈ 63.39	≈ 6.91

Fig. 11. A): DIC snapshots obtained at different loading steps during loading until failure; b): Tensile curves obtained from DIC measurements for different regions: BM, HAZ, weld toe and FZ; c1): Overview of fractured sample; c2): close-up highlighting a ductile-like morphology and dimples of the fractured surface.

plastic, and fracture stages) during tensile testing were taken. Fig. 11a) presents the digital snapshots, while Fig. 11b) depicts the stress-strain curve plots for the analyzed regions, and Fig. 11c) provides a detailed representation of the fractured surface of the welded joint.

In Fig. 11a), the DIC cloud maps provide a clear visualization of strain distribution within the welded joint during tensile testing. During the elastic deformation stage, the strain is initially uniformly distributed throughout the whole joint. As the yield stage is reached, strain begins to be localized at the interface of the HAZ and the FZ (near the weld toe), ultimately leading to stress concentration and fracture failure at the weld toe. The data shown in Fig. 11a) strongly supports the earlier inferences regarding the cause of failure in the welded joint, i.e., t stress concentration at the weld toe. It is worth mentioning that there are two main reasons for this stress concentration to occur: i) the geometric defects due to the presence of face/root reinforcements; ii) the existence of Nb-rich carbides, Laves phases, and σ phases at the interface of the weld toe. These hard precipitates particles act as stress concentrators, further promoting crack formation. Here, an interesting observation is that the strain is larger in the lower HAZ in the third DIC image, while it becomes larger in the upper HAZ in the fourth image. This phenomenon can be attributed to the dynamic evolution of the stress and strain fields during the tensile process. Due to the incomplete symmetry of the weld geometry, such as differences in reinforcement height between the upper and lower sides, and local microstructural variations, the local yielding point shifts during loading, leading to a gradual transfer of the maximum strain concentration region from the lower side to the upper side.

In Fig. 11b), it is evident that different regions of the welded joint exhibit distinct mechanical responses during tensile loading. The BM region shows the highest yield strength and the smallest deformation (≈556 MPa and ≈3.05 %), followed by the FZ (≈478 MPa and ≈6.91 %), the HAZ (≈396 MPa and ≈20.80 %), and finally, the weld toe region with the lowest yield strength and the largest plastic deformation (≈226 MPa and ≈63.39 %). In fact, the different mechanical behaviors exhibited by these regions are primarily determined by the load transfer during the tensile process, as well as the inherent mechanical properties of each region. During tensile testing, the external load is applied to the welded joint, and initially, the softer HAZ and FZ regions tend to bear more load. However, in the FZ, due to the presence of face/root reinforcements increase the load-bearing area, resulting in a decrease in the force borne per unit area. As a result, the HAZ yields before the FZ and exhibits a greater plastic deformation. The BM region, with its high hardness (refer to Fig. 9 b)), dominates the resistance to plastic deformation. Theoretically, once the FZ and HAZ reach yield, the load should start to be transferred to the BM. Interestingly, the weld toe region, due to the presence of geometric defects and hard precipitated phases, is prone to stress concentration, leading to preferential local deformation, as shown by the blue line in Fig. 11b). Therefore, after yielding in the FZ, HAZ, and weld toe regions, there is no significant load transfer to the BM region. Fig. 11c) shows the representative fractured tensile specimen and the corresponding fracture surface. The macroscopic (Fig. 11c1) and high-magnification images (Fig. 11c2)) reveal numerous uniformly distributed dimples, indicating that the welded joint primarily underwent ductile fracture.

3.3. *Strengthening mechanism calculations*

Fig. 12 details the predominant strengthening mechanisms in the BM, HAZ, and FZ of the welded joint, detailing the contributions of solid solution strengthening σ_{SS}, dislocation strengthening σ_{dis}, and Hall-Petch strengthening σ_{HP} to the yield strength of each region. The yield strength of typical regions was determined from the stress-strain curves obtained through DIC analysis. Besides, it is important to mention, considering the significant microstructural differences across the HAZ due to the welding thermal cycle, that the strengthening mechanisms were evaluated using the overall average values for the entire HAZ, rather than focusing on specific localized regions. For the dislocation strengthening mechanism, synchrotron radiation data were used to calculate the dislocation density of the entire welded joint, with further extraction of dislocation density values across all regions of the HAZ. The average dislocation strengthening value was then calculated, representing the overall dislocation strengthening effect in the HAZ. Similarly, for the Hall-Petch strengthening mechanism, grain size data obtained from EBSD were used, which covered the entire HAZ, from the BM to the FZ. The average grain sizes were analyzed to calculate the Hall-Petch strengthening value for the entire HAZ. The same method for calculation the solid-solution strengthening. This approach ensures that the results reflect the comprehensive microstructural characteristics of the HAZ, accounting for the variations across different regions.

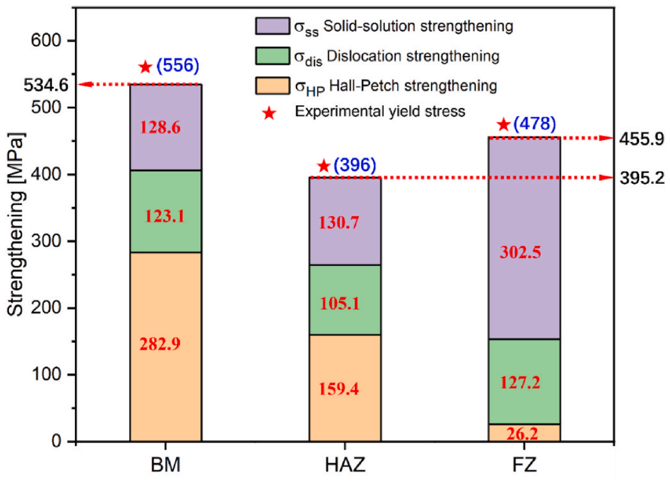

Fig. 12. – Contributions of different strengthening mechanisms to thew yield strength of different regions (BM, HAZ and FZ).

Overall, different regions of the welded joint exhibit distinct primary strengthening mechanisms, which arise from the variations in microstructure and performance at different regions of the material due to the weld thermal. For the BM, σ_{SS}, σ_{dis}, and σ_{HP} contribute approximately ≈128.6 MPa, ≈123.1 MPa, and ≈282.9 MPa, respectively, to a yield strength of nearly ≈556 MPa. Comparing the contributions of these three strengthening mechanisms to the yield strength, it can be observed that Hall-Petch strengthening is the main contributor in this region. Despite the high dislocation density generated during the rolling process in this region (refer to Fig. 3 d)), its contribution to the yield strength is only half of that from Hall-Petch strengthening (123.1 MPa Vs. ≈ 282.9 MPa). This suggests that for equiatomic CoCrFeMnNi HEAs, grain refinement can be a more effective method for strengthening the material. Therefore, it is advisable to select a base metal with smaller grain size prior to welding. As moving into the HAZ, a decrease in the contributions of both Hall-Petch strengthening and dislocation strengthening to the yield strength can be observed. This reduction can be mainly attributed to the impact of the weld thermal cycle in this region, which release the pre-stored strain energy in the BM, resulting in a reduction in dislocation density (refer to Fig. 3 d)) and promoting recrystallization and grain coarsening of the pancake-like fine grains in the BM (refer to Fig. 3 e)). Nevertheless, Hall-Petch strengthening still dominates ($\sigma_{HP} \approx 159.4$ MPa $> \sigma_{ss} \approx 130.7$ MPa $> \sigma_{dis} \approx 105.1$ MPa). Since the weld thermal cycle experienced in the HAZ cannot lead to the elemental redistribution, the solid solution strengthening effect is similar to that in the BM region (≈128.6 MPa Vs. ≈ 130.7 MPa), the slightly variation being due to different Taylor factor values extracted from the EBSD data.

Upon entering the FZ, the dominant strengthening mechanism changes from the dominance of Hall-Petch strengthening in the BM and HAZ regions to solid solution strengthening, which accounts for approximately three-quarters of the total yield strength (≈395.2 MPa

Vs. ≈ 302.5 MPa), while the contribution from Hall-Petch strengthening is only around ≈26.15 MPa, making it the least significant mechanism in terms of yield strength contribution for that given grain size. This transition in strengthening mechanism is expected due to the grain characteristic of the FZ. Solid solution strengthening is primary associated with lattice distortion caused by atomic mismatch, whereas a characteristic feature of the FZ is the redistribution of elements. The filler wire, Inconel 625, contains large elements with atomic radius, namely Nb and Mo, which are also typical solid solution strengthening elements [50,51]. Therefore, it can be inferred that the Nb and Mo elements present in the filler wire injected into the weld pool are the main contributors to the enhanced solid solution strengthening in the FZ. Additionally, the presence of coarse dendritic and columnar grains (refer to Fig. 3 e)) in this region is the main reason for the weakening of the Hall-Petch strengthening mechanism. Interestingly, the contribution of dislocation strengthening in the FZ to the yield strength is comparable to that in the BM (≈127.2 MPa Vs. ≈128.6 MPa). At first glance, this may appear contradictory to the dislocation distribution captured in the BM and FZ through EBSD analysis (refer to Fig. 3 d)). However, this apparent discrepancy is related to the differences in the scanning range between EBSD and synchrotron radiation techniques [52]. The scanning range of EBSD is typically limited to the near-surface region of the sample, providing microstructural information only at the surface layer level, while it fails to capture the bulk dislocation information in this region, such as dislocation changes caused by residual stresses and lattice distortions. However, high energy synchrotron radiation can probe the material through thickness enabling to obtain bulk microstructure information. Moreover, the FZ, being the region directly subjected to the heat source during welding, inevitably experiences thermally induced strains, leading to residual stresses and lattice distortion in the thickness direction after rapid melting and cooling. However, EBSD is unable to capturing such effects in the depth direction due to its own limited scanning range, while synchrotron radiation technique can overcome this limitation and provide a more comprehensive observational capability. Therefore, synchrotron radiation possesses a greater advantage over EBSD when in need to study bulk microstructure and strengthening mechanisms of the FZ. Here, it is important to note that the yield strength model employed in this study did not include a precipitation strengthening term, primarily due to two considerations. First, the mechanical properties of the FZ matrix are difficult to define with precision. The FZ in this work is formed through the complete melting and mixing of Inconel 625 and CoCrFeMnNi HEA, resulting in a complex multi-component solid solution. The crystal structure and key mechanical parameters of this region - such as shear modulus (G), Burger's vector (b), and Poisson's ratio (ν) - are challenging to determine accurately. Without these critical parameters, applying the Orowan mechanism to quantify precipitation strengthening could introduce significant uncertainties, thereby undermining the reliability of the model. Moreover, approximating the mechanical properties of the FZ by simply adopting those of either Inconel 625 or CoCrFeMnNi HEA would involve considerable assumptions and could compromise the model's validity. To maintain the scientific rigor and credibility of the model, precipitation strengthening was therefore not explicitly incorporated in the yield strength calculation. Second, although precipitation strengthening was not directly calculated, its effect was indirectly considered through the dislocation strengthening mechanism. As discussed earlier, Nb-induced precipitates were primarily observed along grain boundaries in the FZ, where they acted as dislocation pinning sites. Their presence impeded dislocation motion, promoted dislocation accumulation, and increased the overall dislocation density - thereby enhancing the contribution of dislocation strengthening. Quantitative analysis of the strengthening mechanisms further confirmed that dislocation strengthening was the second most significant contributor to the yield strength in the FZ. Thus, although the Orowan-based precipitation strengthening was not explicitly included in the model, the precipitates still indirectly enhanced the mechanical strength by facilitating dislocation pile-up. This contribution is further elaborated upon in the strengthening mechanism analysis section.

In conclusion, the linear summed strengthening effects obtained are approximately ≈534.55 MPa (BM), ≈395.22 MPa (HAZ), and ≈456.86 MPa (FZ), which are slightly lower than the experimentally obtained yield strengths in each region. This discrepancy between the calculated and experimental values can be attributed to the presence of precipitate phases.

4. Conclusions

This work conducted an in-depth investigation into the weldability of a gas metal arc welded joint of CoCrFeMnNi HEA using Inconel 625 filler wire, as well as a comprehensive analysis of strengthening mechanisms in different typical regions of the welded joints. The following conclusions can be drawn.

1) Overall, the gas metal arc welded CoCrFeMnNi joints with the addition of Inconel 625 filler wire exhibits excellent welding performance, and no welding defects were observed, indicating a favorable metallurgical interaction between the Inconel 625 filler and the CoCrFeMnNi HEA.
2) The different regions of the welded joint exhibit distinct microstructural features due to the weld thermal cycle. The observed recrystallization phenomenon as well as the coarsening of the grain structure was evidenced leading to a softening effect in the HAZ.
3) The Scheil-Gulliver model can be utilized to predict the solidification path and phase structure of the FZ. The results obtained from this model showed good agreement with microscopy- and synchrotron-based measurements.
4) The strain distribution during tensile loading of the joints shows a significant localization during the tensile testing of the joint. In the elastic stage, the strain is uniformly distributed. However, after reaching the yield point, the strain gradually localizes towards the interface of the HAZ and FZ.
5) The stress concentration at the weld toe is the primary cause of failure in welded joints, and this stress concentration at the toe originates from geometric imperfections in the face/root reinforcement and the presence of hard precipitated phases.
6) Different regions of the welded joint (BM, HAZ and FZ) exhibit different primary strengthening mechanisms. Hall-Petch strengthening is the main contributor to the yield stress in the BM and HAZ, while solid-solution strengthening is predominant in the FZ.

CRediT authorship contribution statement

Jiajia Shen: Writing – original draft, Methodology, Investigation, Formal analysis. **Jin Yang:** Investigation. **Yeon Taek Choi:** Investigation. **Rita Gonçalves:** Investigation. **Rodrigo Pedro:** Investigation. **D. A. Santana:** Investigation. **F.G. Coury:** Investigation. **N. Schell:** Investigation. **Zhi Zeng:** Investigation. **Hyoung Seop Kim:** Validation, Formal analysis. **J.P. Oliveira:** Writing – review & editing, Validation, Supervision, Formal analysis, Conceptualization.

Declaration of competing interest

The authors declare that they have no known competing financial interests or personal relationships that could have appeared to influence the work reported in this paper.

Acknowledgments

JS and JPO acknowledge Fundação para a Ciência e a Tecnologia (FCT - MCTES) for its financial support via the project UID/00667/2020 (UNIDEMI). JS and JPO acknowledges the funding of CENIMAT/i3N by national funds through the FCT-Fundação para a Ciência e a Tecnologia, I.P., within the scope of LA/P/0037/2020, UIDP/50025/2020 and UIDB/50025/2020 of the Associate Laboratory Institute of Nanostructures, Nanomodelling and Nanofabrication – i3N. JS acknowledges the China Scholarship Council for funding the Ph.D. grant (CSC NO. 201808320394). This work was supported by the National Research Foundation of Korea (NRF) with a grant funded by the Korea government (MSIP) (NRF-2021R1A2C3006662). The authors acknowledge DESY (Hamburg, Germany), a member of the Helmholtz Association HGF, for the provision of experimental facilities. Beamtime was allocated for proposal I-20210899 EC. The research leading to this result has been supported by the project CALIPSOplus under the Grant Agreement 730872 from the EU Framework Programme for Research and Innovation HORIZON 2020.

Appendix A. Supplementary data

Supplementary data to this article can be found online at https://doi.org/10.1016/j.msea.2025.148452.

Data availability

Data will be made available on request.

References

[1] J.-W. Yeh, S.-K. Chen, S.-J. Lin, J.-Y. Gan, T.-S. Chin, T.-T. Shun, C.-H. Tsau, S.-Y. Chang, Nanostructured high-entropy alloys with multiple principal elements: novel alloy design concepts and outcomes, Adv. Eng. Mater. 6 (2004) 299–303, https://doi.org/10.1002/adem.200300567.

[2] B. Cantor, I.T.H. Chang, P. Knight, A.J.B. Vincent, Microstructural development in equiatomic multicomponent alloys, Mater. Sci. Eng. A 375–377 (2004) 213–218, https://doi.org/10.1016/j.msea.2003.10.257.

[3] A. Huang, S.J. Fensin, M.A. Meyers, Strain-rate effects and dynamic behavior of high entropy alloys, J. Mater. Res. Technol. 22 (2023) 307–347, https://doi.org/10.1016/j.jmrt.2022.11.057.

[4] Z. Wu, S.A. David, Z. Feng, H. Bei, Weldability of a high entropy CrMnFeCoNi alloy, Scr. Mater. 124 (2016) 81–85, https://doi.org/10.1016/j.scriptamat.2016.06.046.

[5] Y. Palguna, K. Sairam, A.R. Kannan, N.S. Shanmugam, R. Korla, J.P. Oliveira, Effect of post weld heat treatment on the microstructure and mechanical properties of gas tungsten arc welded Al0.3CoCrFeNi high entropy alloy, Scr. Mater. 241 (2024) 115887, https://doi.org/10.1016/j.scriptamat.2023.115887.

[6] N. Kashaev, V. Ventzke, N. Stepanov, D. Shaysultanov, V. Sanin, S. Zherebtsov, Laser beam welding of a CoCrFeNiMn-type high entropy alloy produced by self-propagating high-temperature synthesis, Intermetallics 96 (2018) 63–71, https://doi.org/10.1016/j.intermet.2018.02.014.

[7] M.-G. Jo, H.-J. Kim, M. Kang, P.P. Madakashira, E.S. Park, J.-Y. Suh, D.-I. Kim, S.-T. Hong, H.N. Han, Microstructure and mechanical properties of friction stir welded and laser welded high entropy alloy CrMnFeCoNi, Met. Mater. Int. 24 (2018) 73–83, https://doi.org/10.1007/s12540-017-7248-x.

[8] S.S. Nene, K. Liu, M. Frank, R.S. Mishra, R.E. Brennan, K.C. Cho, Z. Li, D. Raabe, Enhanced strength and ductility in a friction stir processing engineered dual phase high entropy alloy, Sci. Rep. 7 (2017) 16167, https://doi.org/10.1038/s41598-017-16509-9.

[9] Y. Hu, Y. Niu, Y. Zhao, W. Yang, X. Ma, J. Li, Friction stir welding of CoCrNi medium-entropy alloy: recrystallization behaviour and strengthening mechanism, Mater. Sci. Eng. A 848 (2022) 143361, https://doi.org/10.1016/j.msea.2022.143361.

[10] N.K. Adomako, G. Shin, N. Park, K. Park, J.H. Kim, Laser dissimilar welding of CoCrFeMnNi-high entropy alloy and duplex stainless steel, J. Mater. Sci. Technol. 85 (2021) 95–105, https://doi.org/10.1016/j.jmst.2021.02.003.

[11] R.H. Buzolin, T. Richter, F. Pixner, M. Rhode, D. Schroepfer, N. Enzinger, Microstructure and texture characterisation of friction stir welded CoCrNi and CoCrFeMnNi multi-principle element alloys, Mater. Today Commun. 35 (2023) 105870, https://doi.org/10.1016/j.mtcomm.2023.105870.

[12] H. Nam, S. Park, N. Park, Y. Na, H. Kim, S.-J. Yoo, Y.-H. Moon, N. Kang, Weldability of cast CoCrFeMnNi high-entropy alloys using various filler metals for cryogenic applications, J. Alloys Compd. 819 (2020) 153278, https://doi.org/10.1016/j.jallcom.2019.153278.

[13] J.P. Oliveira, J. Shen, Z. Zeng, J.M. Park, Y.T. Choi, N. Schell, E. Maawad, N. Zhou, H.S. Kim, Dissimilar laser welding of a CoCrFeMnNi high entropy alloy to 316 stainless steel, Scr. Mater. 206 (2022) 114219, https://doi.org/10.1016/j.scriptamat.2021.114219.

[14] J.P. Oliveira, A. Shamsolhodaei, J. Shen, J.G. Lopes, R.M. Gonçalves, M. de Brito Ferraz, L. Piçarra, Z. Zeng, N. Schell, N. Zhou, H. Seop Kim, Improving the ductility in laser welded joints of CoCrFeMnNi high entropy alloy to 316 stainless steel, Mater. Des. 219 (2022) 110717, https://doi.org/10.1016/j.matdes.2022.110717.

[15] P. Chen, C. Yang, S. Li, M.M. Attallah, M. Yan, In-situ alloyed, oxide-dispersion-strengthened CoCrFeMnNi high entropy alloy fabricated via laser powder bed fusion, Mater. Des. 194 (2020) 108966, https://doi.org/10.1016/j.matdes.2020.108966.

[16] Y. Han, H. Li, H. Feng, Y. Tian, Z. Jiang, T. He, Mechanism of dislocation evolution during plastic deformation of nitrogen-doped CoCrFeMnNi high-entropy alloy, Mater. Sci. Eng. A 814 (2021) 141235, https://doi.org/10.1016/j.msea.2021.141235.

[17] P. Zhang, Y. Qi, Q. Cheng, X. Sun, Welding dissimilar alloys of CoCrFeMnNi high-entropy alloy and 304 stainless steel using gas tungsten arc welding, J. Mater. Eng. Perform. 33 (2024) 3273–3282, https://doi.org/10.1007/s11665-023-08229-1.

[18] H. Nam, S. Yoo, J. Lee, Y. Na, N. Park, N. Kang, GTA weldability of rolled high-entropy alloys using various filler metals, Metals 10 (2020) 1371, https://doi.org/10.3390/met10101371.

[19] H. Nam, S. Yoo, J.W. Ha, B.-J. Lee, S. Song, Y. Na, N. Kang, Enhancement of tensile properties of gas tungsten arc welds using Cu-coated CoCrFeMnNi filler and post–weld heat treatment, J. Mater. Res. Technol. 19 (2022) 4857–4866, https://doi.org/10.1016/j.jmrt.2022.07.023.

[20] J.M. Park, E.S. Kim, H. Kwon, P. Sathiyamoorthi, K.T. Kim, J.-H. Yu, H.S. Kim, Effect of heat treatment on microstructural heterogeneity and mechanical properties of 1%C-CoCrFeMnNi alloy fabricated by selective laser melting, Addit. Manuf. 47 (2021) 102283, https://doi.org/10.1016/j.addma.2021.102283.

[21] D. Yim, P. Sathiyamoorthi, S.-J. Hong, H.S. Kim, Fabrication and mechanical properties of TiC reinforced CoCrFeMnNi high-entropy alloy composite by water atomization and spark plasma sintering, J. Alloys Compd. 781 (2019) 389–396, https://doi.org/10.1016/j.jallcom.2018.12.119.

[22] H.Y. Yasuda, K. Shigeno, T. Nagase, Dynamic strain aging of Al 0.3 CoCrFeNi high entropy alloy single crystals, Scr. Mater. 108 (2015) 80–83, https://doi.org/10.1016/j.scriptamat.2015.06.022.

[23] J. Shen, J.G. Lopes, Z. Zeng, Y.T. Choi, E. Maawad, N. Schell, H.S. Kim, R.S. Mishra, J.P. Oliveira, Deformation behavior and strengthening effects of an eutectic AlCoCrFeNi2.1 high entropy alloy probed by in-situ synchrotron X-ray diffraction and post-mortem EBSD, Mater. Sci. Eng. A 872 (2023) 144946, https://doi.org/10.1016/j.msea.2023.144946.

[24] G. Williamson, W. Hall, X-ray line broadening from filed aluminium and wolfram, Acta Metall. 1 (1953) 22–31, https://doi.org/10.1016/0001-6160(53)90006-6.

[25] C. Varvenne, A. Luque, W.A. Curtin, Theory of strengthening in fcc high entropy alloys, Acta Mater. 118 (2016) 164–176, https://doi.org/10.1016/j.actamat.2016.07.040.

[26] D. de Araujo Santana, C.S. Kiminami, F.G. Coury, Mechanical properties and yield strength modeling of a medium entropy alloy containing L12 precipitates, J. Alloys Compd. 898 (2022) 162923, https://doi.org/10.1016/j.jallcom.2021.162923.

[27] G.F. Kayser, The lattice parameters and microstructures of annealed, nickel-rich nickel-molybdenum alloys, J. Mater. Sci. 24 (1989) 2677–2680, https://doi.org/10.1007/BF02385610.

[28] S. Arajs, H. Chessin, R.V. Colvin, Lattice parameters and paramagnetic susceptibility of nickel-rich nickel-niobium solid solutions, Phys. Status Solidi 3 (1963) 2337–2346, https://doi.org/10.1002/pssb.19630031216.

[29] D. Molochkov, R. Kulykovskyi, Compensation of filler wire deflection in robotic gas metal arc welding processes, Weld. World 68 (2024) 2805–2818, https://doi.org/10.1007/s40194-024-01810-9.

[30] M. Ma, R. Lai, J. Qin, B. Wang, H. Liu, D. Yi, Effect of weld reinforcement on tensile and fatigue properties of 5083 aluminum metal inert gas (MIG) welded joint: experiments and numerical simulations, Int. J. Fatig. 144 (2021) 106046, https://doi.org/10.1016/j.ijfatigue.2020.106046.

[31] J. Shen, R. Gonçalves, Y.T. Choi, J.G. Lopes, J. Yang, N. Schell, H.S. Kim, J. P. Oliveira, Microstructure and mechanical properties of gas metal arc welded CoCrFeMnNi joints using a 308 stainless steel filler metal, Scr. Mater. 222 (2023) 115053, https://doi.org/10.1016/j.scriptamat.2022.115053.

[32] J.P. Oliveira, T.M. Curado, Z. Zeng, J.G. Lopes, E. Rossinyol, J.M. Park, N. Schell, F. M. Braz Fernandes, H.S. Kim, Gas tungsten arc welding of as-rolled CrMnFeCoNi high entropy alloy, Mater. Des. 189 (2020) 108505, https://doi.org/10.1016/j.matdes.2020.108505.

[33] X.-M. Chen, Y.C. Lin, F. Wu, EBSD study of grain growth behavior and annealing twin evolution after full recrystallization in a nickel-based superalloy, J. Alloys Compd. 724 (2017) 198–207, https://doi.org/10.1016/j.jallcom.2017.07.027.

[34] B. Gludovatz, A. Hohenwarter, D. Catoor, E.H. Chang, E.P. George, R.O. Ritchie, A fracture-resistant high-entropy alloy for cryogenic applications, Science 345 (2014) 1153–1158, https://doi.org/10.1126/science.1254581.

[35] J.P. Oliveira, D. Barbosa, F.M.B. Fernandes, R.M. Miranda, Tungsten inert gas (TIG) welding of Ni-rich NiTi plates: functional behavior, Smart Mater. Struct. 25 (2016) 03LT01, https://doi.org/10.1088/0964-1726/25/3/03LT01.

[36] G. Qin, Z. Li, R. Chen, H. Zheng, C. Fan, L. Wang, Y. Su, H. Ding, J. Guo, H. Fu, CoCrFeMnNi high-entropy alloys reinforced with laves phase by adding Nb and Ti elements, J. Mater. Res. 34 (2019) 1011–1020, https://doi.org/10.1557/jmr.2018.468.

[37] G. Qin, R. Chen, H. Zheng, H. Fang, L. Wang, Y. Su, J. Guo, H. Fu, Strengthening FCC-CoCrFeMnNi high entropy alloys by Mo addition, J. Mater. Sci. Technol. 35 (2019) 578–583, https://doi.org/10.1016/j.jmst.2018.10.009.

[38] S. Li, Q. Wei, Y. Shi, Z. Zhu, D. Zhang, Microstructure characteristics of inconel 625 superalloy manufactured by selective laser melting, J. Mater. Sci. Technol. 31 (2015) 946–952, https://doi.org/10.1016/j.jmst.2014.09.020.

[39] M. Shakil, M. Ahmad, N.H. Tariq, B.A. Hasan, J.I. Akhter, E. Ahmed, M. Mehmood, M.A. Choudhry, M. Iqbal, Microstructure and hardness studies of electron beam welded Inconel 625 and stainless steel 304L, Vacuum 110 (2014) 121–126, https://doi.org/10.1016/j.vacuum.2014.08.016.

[40] H. Jiang, L. Li, Z. Ni, D. Qiao, Q. Zhang, H. Sui, Effect of Nb on microstructure and properties of AlCoCrFeNi2.1 high entropy alloy, Mater. Chem. Phys. 290 (2022) 126631, https://doi.org/10.1016/j.matchemphys.2022.126631.

[41] Y. Hu, X. Lin, Y. Li, S. Zhang, Q. Zhang, W. Chen, W. Li, W. Huang, Influence of heat treatments on the microstructure and mechanical properties of Inconel 625 fabricated by directed energy deposition, Mater. Sci. Eng. A 817 (2021) 141309, https://doi.org/10.1016/j.msea.2021.141309.

[42] S. Huang, H. Wu, H. Zhu, Z. Xie, Effect of niobium addition upon microstructure and tensile properties of CrMnFeCoNix high entropy alloys, Mater. Sci. Eng. A 809 (2021) 140959, https://doi.org/10.1016/j.msea.2021.140959.

[43] R. Li, J. Ren, G.-J. Zhang, J.-Y. He, Y.-P. Lu, T.-M. Wang, T.-J. Li, Novel (CoFe2NiV0.5Mo0.2)100−xNbx eutectic high-entropy alloys with excellent combination of mechanical and corrosion properties, Acta Metall. Sin. (English Lett. 33 (2020) 1046–1056, https://doi.org/10.1007/s40195-020-01072-6.

[44] Y. Chen, M. Xu, T. Zhang, J. Xie, K. Wei, S. Wang, L. Yin, P. He, Grain refinement and mechanical properties improvement of Inconel 625 alloy fabricated by ultrasonic-assisted wire and arc additive manufacturing, J. Alloys Compd. 910 (2022) 164957, https://doi.org/10.1016/j.jallcom.2022.164957.

[45] A. Kruk, G. Cempura, Decomposition of the Laves phase in the fusion zone of the Inconel 718/ATI 718Plus® welded joint during isothermal holding at a temperature of 649 °C, Mater. Charact. 196 (2023) 112560, https://doi.org/10.1016/j.matchar.2022.112560.

[46] J. Shen, R. Gonçalves, Y.T. Choi, J.G. Lopes, J. Yang, N. Schell, H.S. Kim, J. P. Oliveira, Microstructure and mechanical properties of gas metal arc welded CoCrFeMnNi joints using a 410 stainless steel filler metal, Mater. Sci. Eng. A 857 (2022) 144025, https://doi.org/10.1016/j.msea.2022.144025.

[47] Y.L. Hu, X. Lin, S.Y. Zhang, Y.M. Jiang, X.F. Lu, H.O. Yang, W.D. Huang, Effect of solution heat treatment on the microstructure and mechanical properties of Inconel 625 superalloy fabricated by laser solid forming, J. Alloys Compd. 767 (2018) 330–344, https://doi.org/10.1016/j.jallcom.2018.07.087.

[48] R. Sokkalingam, B. Pravallika, K. Sivaprasad, V. Muthupandi, K.G. Prashanth, Dissimilar welding of high-entropy alloy to Inconel 718 superalloy for structural applications, J. Mater. Res. 37 (2022) 272–283, https://doi.org/10.1557/s43578-021-00352-w.

[49] H. Shah Hosseini, M. Shamanian, A. Kermanpur, Microstructural and weldability analysis of Inconel617/AISI 310 stainless steel dissimilar welds, Int. J. Pres. Ves. Pip. 144 (2016) 18–24, https://doi.org/10.1016/j.ijpvp.2016.05.004.

[50] U. Gürol, M. Tümer, S. Dilibal, Experimental investigation of wire Arc additively manufactured inconel 625 superalloy, Trans. Indian Inst. Met. 76 (2023) 1371–1379, https://doi.org/10.1007/s12666-022-02797-x.

[51] F. Zhang, C. Wang, Y. Wu, L. Zhou, Q. Tian, Microstructural stability and mechanical properties of GH742 Ni-based wrought superalloy for turbine disk applications, Mater. Sci. Eng. A 832 (2022) 142488, https://doi.org/10.1016/j.msea.2021.142488.

[52] L.H.M. Antunes, J.J. Hoyos, T.C. Andrade, P.W.C. Sarvezuk, L. Wu, J.A. Ávila, J. P. Oliveira, N. Schell, A.L. Jardini, J. Žilková, P.F. da Silva Farina, H.F.G. Abreu, M. Béreš, Deformation-induced martensitic transformation in Co-28Cr-6Mo alloy produced by laser powder bed fusion: Comparison surface vs. bulk, Addit. Manuf. 46 (2021) 102100, https://doi.org/10.1016/j.addma.2021.102100.